HIGH-RESOLUTION BALL LENS-ASSISTED IMAGING

By

Amstrong Renold Jean

A thesis submitted to the faculty of
The University of North Carolina at Charlotte
in partial fulfillment of the requirements
for the degree of Master of Science in
Optical Science and Engineering.

Charlotte

2024

Approved by:

_____
Dr. Vasily Astratov

_____
Dr. Rosario Porras-Aguilar

_____
Dr. Yuri Nesmelov

ABSTRACT

AMSTRONG RENOLD JEAN. High-Resolution Ball Lens-Assisted Imaging.
(Under the direction of DR. VASILY ASTRATOV)

Cellphone-based microscopes attract significant attention due to their application in portable and lightweight systems operating without heavy microscope stands and bulky objectives. However, the resolution of cellphone-based microscopes is typically pixel-limited due to insufficient image magnification. An increase in magnification usually comes at the expense of field-of-view (FoV). In this thesis work, we develop cellphone-based microscopy by integrating cellphones with high-index ball lenses placed in a contact position with the investigated nanoplasmonic objects. Due to extremely high additional image magnification provided for real or virtual images depending on the refractive index of the ball lenses, a significant resolution advantage over more conventional systems was realized allowing in principle to overcome the pixelation problem and to make a step towards achieving diffraction-limited resolution by ordinary cell phone. It is shown that this goal can be achieved using ball lenses with a specially designed index of refraction, typically being sufficiently close to an index of about two. To increase FoV, we developed the technology of thermal pressure embedding of highly ordered arrays of ball lenses with different diameters in plastic coverslips. For the same purpose, we developed technology for translating ball lenses along the surface of investigated samples followed by stitching corresponding images. The resolution of cellphone-based microscopy obtained through movable ball lenses is estimated to be at approximately 1.5 μm level, but we see potential to reach the diffraction-limited resolution over a millimeter-scale FoV by the cellphone-based imaging in future studies.

ACKNOWLEDGEMENT

I am profoundly grateful to extend my sincere appreciation to my esteemed advisor, Dr. Vasily N. Astratov, whose tireless support has been instrumental in shaping my academic journey and my perspective on life over the past two years. Dr. Astratov's unmatched expertise and wisdom have profoundly impacted me. Without his guidance, encouragement, and insights, the fruition of the work presented in this thesis would have remained an obscure dream. Dr. Astratov's mentorship has not only enhanced my understanding of good scientific research but has also instilled in me a deep sense of confidence propelling me forward in my future endeavors. I am deeply indebted to him for his constant belief in my potential and his devoted commitment to my success.

Furthermore, I wish to express my deepest gratitude to Dr. Rosario Porras-Aguilar and Dr. Yuri Nesmelov for kindly agreeing to participate in my dissertation committee. Their commitment to devoting their time and sharing their expertise has been essential to the outcome of my dissertation. Their constructive criticism and invaluable feedback have greatly improved the quality of my research, and I am deeply appreciative of their support and guidance.

In addition, I am grateful to Dr. Glenn Boreman and Dr. Tino Hofmann for their support and dedication throughout every stage of my academic journey. Their support and willingness to help have been instrumental in shaping my academic and personal growth. Their contributions have left a lasting mark, and I am truly fortunate to have had their support every step of the way.

I extend my gratitude to Dr. Menelaos Poutous, Dr. Greg Gbur, Dr. Yildirim Aktas, and Dr. Tsing-Hua Her for their assistance, enlightening discussions, and insights that have enriched my academic journey. Their guidance has helped shape my educational experience. I am sincerely appreciative of their commitment which has contributed significantly to my development.

I express my gratitude to Dr. Lou Deguzman and Scott Williams for their help and training. Their training has helped shape my research experience. Additionally, I extend my thanks to Renee Johnson for her dedicated support with administrative tasks, which has greatly facilitated the smooth progress of my work. I am deeply appreciative of their collective contributions, which have played a pivotal role in my growth and success.

During my time in graduate school, receiving the GASP award was incredibly important, and I am extremely grateful for it. I want to express my deep appreciation to the Department of Physics and Optical Sciences for offering me teaching assistantships, which have enriched my educational experience. I also give thanks to Vasily N. Astratov, Ph.D., who offered me a position as a research assistant through his grants, without which, my research would not have been possible.

Lastly, I express deep appreciation to my family; their encouragement has been my source of strength throughout this endeavor.

DEDICATION

I dedicated this thesis to my…

…. Family, especially my late father who has played a pivotal role in my life,

…my brother for his encouragement and support.

…good friends Nicholas Emanuel and Elizabeth Vargas.

TABLE OF CONTENTS

LIST OF FIGURES

LIST OF ABBREVIATIONS

NA	numerical aperture
PSF	point-spread function
FL	fluorescent
MAM	microsphere-assisted microscopy
SIL	solid immersion lens
BTG	barium titanate glass
IPA	isopropyl alcohol
SEM	scanning electron microscope
BD	blu ray disc
FOV	field-of-view
NPD	nanoplasmonic arrays of dimers,
M	magnification
D	diameter
PDMS	polydimethylsiloxane
FSB	fused silica balls
CD	compact dis

CHAPTER 1: INTRODUCTION

1.1. Classical diffraction limit in microscopy

In the field of optics, every optical instrument or system faces a fundamental constraint on its resolution, originating from the phenomenon of diffraction dictated by the laws of physics. When an optical instrument achieves its peak resolution performance, it is deemed a diffraction barrier or limited. In the case of microscopic instruments, the spatial resolution constrained by diffraction is directly linked to the wavelength of light and the numerical aperture of either the objective or the object illumination source, depending on which is smaller. The challenge of observing sub-wavelength structures with microscopes arises due to diffraction. In 1873, Ernest Abbe elucidated that light with a wavelength (λ) traveling through a medium with a refractive index (n) and converging to a spot with a half-angle (θ) would encounter a minimum resolvable distance (d) [1]. This finding highlights the inherent limitations imposed by diffraction, which hinder the observation of structures smaller than the wavelength of light. Consequently, achieving higher resolution in optical microscopy necessitates innovative techniques and advancements that push beyond the boundaries set by diffraction, thereby enabling the visualization of increasingly finer details in microscopic specimens.

$$d = \frac{\lambda}{2n\mathrm{Sin}\theta} = \frac{\lambda}{2NA} \qquad (1)$$

In this formula, we used a definition of the numerical aperture (NA) of the microscope objective, NA=2$n$sinθ. According to diffraction theory, images are constructed from an arrangement of diffraction-limited spots with varying intensities, overlapping to generate the resultant image, as previously explained. Thus, the only approach to increase spatial resolution and image contrast is by decreasing the size of these diffraction-limited spots. This reduction can

be done by reducing the imaging wavelength, increasing the numerical aperture, or utilizing a medium with a higher refractive index for imaging. Despite the use of the best objectives under the best of circumstances, lateral resolution remains limited to relatively moderate levels nearing 200 to 250 nanometers due to the transmission properties of glass at wavelengths below 400 nanometers and the inherent constraints on numerical aperture. In contrast, the axial dimension of the Airy disk forms an elliptical pattern often termed the point-spread function (PSF). The elongated structure of the point-spread function along the optical axis arises from the asymmetrical nature of the wavefront emerging from the microscope objective. Axial resolution in optical microscopy is further compromised compared to lateral resolution, typically on the order of 500 nanometers. When endeavoring to image intricately convoluted features such as cellular organelles, the limitations of diffraction-limited resolution become apparent as poor axial sectioning capability and diminished contrast in the imaging plane.

The optical microscopy can be divided into fluorescent (FL) microscopy dealing with biomedical or other samples stained with FL dye molecules or other local emitters [2,3] and label-free microscopy which does not use staining and rely on scattering or absorption of light by the investigated objects [4,5]. In FL microscopy, the resolution can be increased beyond the classical diffraction limit by a variety of methods using stochastic or nonlinear properties of local emitters. The description of these methods goes beyond the scope of this work. In contrast, overcoming the classical diffraction limit in label-free microscopy represents in general a more difficult task since the efficiency of light scattering by nanoscale objects is extremely weak.

According to the Rayleigh criterion, the resolution of two-point sources observed through a microscope is achieved when the central spot of the Airy disk (as depicted in Figure 1) from one point source matches with the first minimum of the Airy disk from the other point source. If the separation between the two Airy disks or point-spread functions exceeds this limit, the point sources are considered resolved, and thus we can say distinguishable. On the contrary, if the distance falls below this value, the Airy disks merge, indicating unresolved point sources. In simpler terms, the Rayleigh criterion is met when the distance between the images of closely spaced point sources is approximately equal to the width of the point-spread function (PSF).

The PSF concept is important in imaging since it is related to the intensity distribution in the image of a single point source. Such intensity distribution can be "projected" back onto the object plane by considering the magnification of the optical system. Such "projected" intensity distribution is clearly representative of the resolution of the system. As an example, if this distribution is approximated by the Gaussian function, the full width at the half maximum of this distribution can be associated with the optical resolution of the system.

In contrast, the Sparrow resolution limit marks the distance between two-point sources where their images no longer exhibit a dip in brightness between the central peaks but maintain constant brightness across the region separating them. The Sparrow resolution limit closely approximates the Abbe value and is approximately two-thirds of the Rayleigh resolution limit, as defined by the Equation.

$$d = \frac{0.61\lambda}{\mathrm{NA}} \quad (Rayleigh\ limit)$$

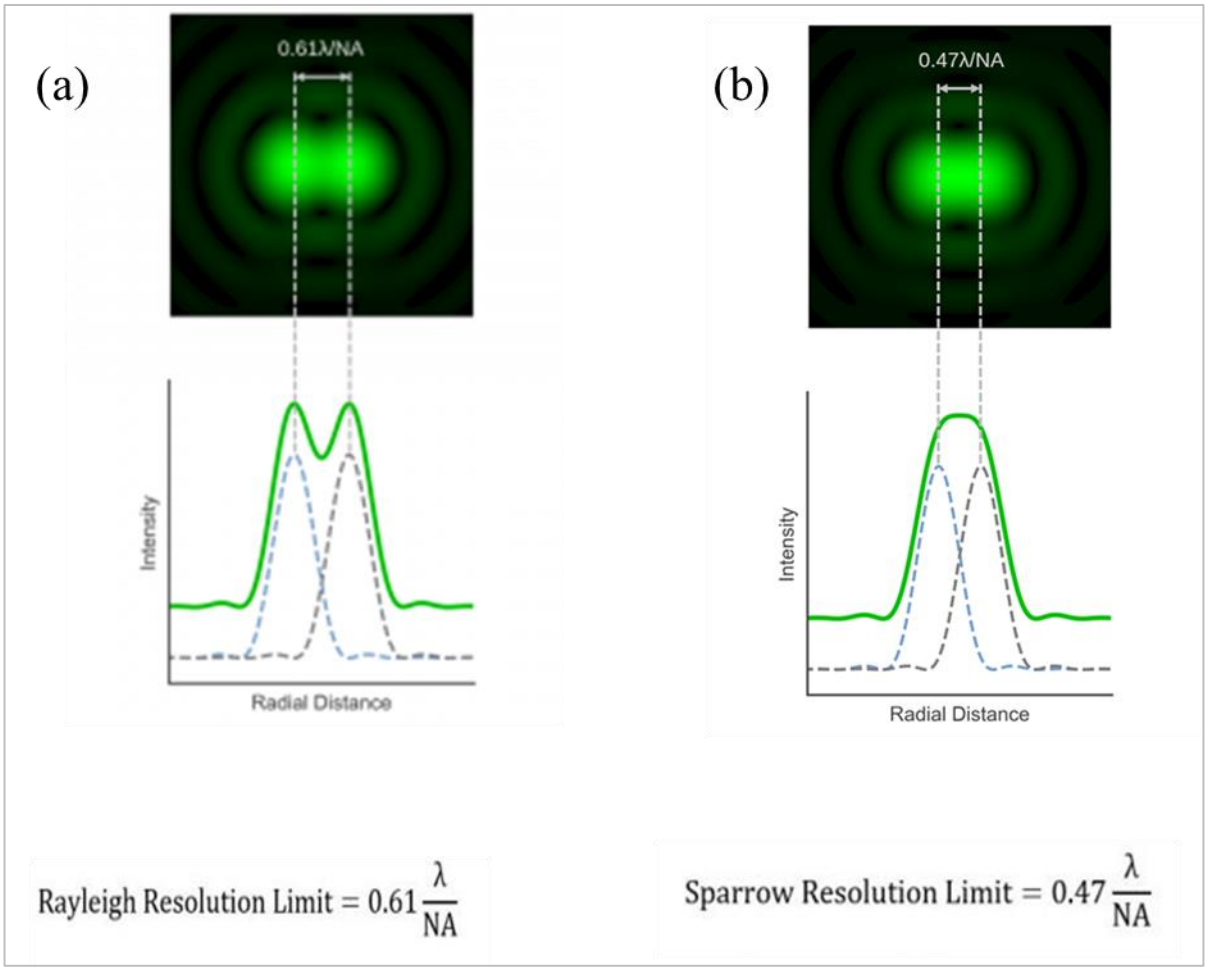

Figure 1: Resolution criterion. (a)Two points positioned at a distance equal to the Rayleigh resolution limit. (b)Two points are positioned at a distance equal to the Sparrow resolution limit. https://www.edinst.com/ko/news/the-rayleigh-criterion-for-microscope-resolution/

1.2. Microsphere-assisted Imaging

Light microscopy stands out as an incredibly potent method for observing specimens in real-time without causing damage, pushing the boundaries of human vision. However, the spatial resolution of traditional microscopes faces a fundamental constraint—the diffraction of light waves at the lens aperture [6]. Over the past decade, microsphere-assisted microscopy (MAM) has emerged as a remarkably simple yet effective technique to overcome this limitation and enhance imaging resolution. This method was used for imaging plasmonic nanostructures

[7,8,9,10], viruses [11], and computer chips [12]. It also provided an increase in the resolution of confocal microscopy [13,14].

The field of micro-spherical nanoscopy is attracting significant attention due to two key factors. To begin with, its simplicity allows for broad applications in imaging subcellular structures, biological molecules, and plasmonic structures. Secondly, the method can achieve resolution values surpassing the diffraction limit. The current focus is on understanding the fundamental reasons behind its super-resolution capability [76]. The experimental resolution is influenced by various factors, including (a) the type of object—near fields can be resonantly enhanced in nanoplasmonic structures; (b) the refractive indexes of the microlens and the surrounding medium—optimal index contrast for virtual imaging falls within the 1.3–1.7 range, but higher average indexes of the microsphere-medium system can enhance resolution.

Microsphere imaging has shown a resolution advantage over conventional microscopy when observing various nanostructures [77,81] and biological entities [82,84]. However, a persistent challenge in microsphere imaging lies in quantifying its resolution. Primarily relying on visual analysis of experimental images has resulted in a wide spectrum of super-resolution claims ranging from $\lambda/6$ to $\lambda/17$ [77,79,81, 84]. A more stringent resolution assessment of metal dimers and bowties, based on the convolution of their shape and the point spread function, yielded a resolution estimate of $\lambda/7$ [85–87]. Notably, this value surpasses the classical upper limit $\lambda/(2\ n) \approx \lambda/4$ in the presence of high-index ($n \approx 2.0$) spheres.

In general, cases overcoming the classical diffraction limit in microscopy can be explained by factors that go beyond the physical model of far-field diffraction. As an example, it can be achieved by scanning the objects' optical near fields using nanoscale probes. It can also be achieved using prior knowledge about the objects or nonlinear optics effects. Alternatively, it can be achieved using contact super-lenses which can preserve or amplify the detailed information about the objects encoded in their optical near fields.

The realization of the optical super-resolution in MAM is rather unusual because it does not involve these factors directly. It should be noted, however, that the microsphere is placed in contact with the object, and, in this sense, it experiences the object's optical near fields. However, this is not sufficient to explain the super-resolution ability of MAM. Only rigorous theory based on the numerical solution of Maxwell equations can shed light on the mechanisms of high-resolution imaging achieved in this method. One obvious factor that can potentially play a role is related to solid immersion lens (SIL) which was initially introduced for hemispherical ball lenses [90], however recently it was shown that in the case of using ball lenses with spherical shapes large-angle waves become trapped inside the microsphere due to the total internal reflection, and, therefore, NA does not increase [15].

A large number of theoretical papers devoted to the resolution capability of MAM were published based on rigorous solutions of the Maxwell equation during the last decade [16-21]. Many factors were considered in these studies including sharply focused beams, so-called "photonic nanojets", whispering gallery modes (WGMs) in microspheres, and polarization properties of the dipole sources. However, the resolution was generally limited by approximately

λ/4 in these studies. Thus, there was no convincing theoretical proof of the resolution at the level of λ/7 expected based on the results of the experimental studies. Only very recently, the super-resolution capability of dielectric microspheres was clearly and unambiguously demonstrated by exact theoretical modeling results [22]. A classical double-slit object was selected for this work. This object was illuminated with a series of plane waves incident from a wide range of directions. The coherent virtual images produced by individual plane waves were found to be not reminiscent of the object. It was shown, however, that the incoherent superposition of many partial images produced by multiple incident plane waves leads to the image reconstruction with a resolution exceeding that of the incoherent imaging theory. It was shown that an essential feature of the super-resolution mechanism is connected to the coherent scattering of the incident waves into the waves circulating around the spherical boundary inside the microspheres. They are trapped inside the microsphere due to total internal reflection. This trapping is an important feature of the mechanism of super-resolution because it provides re-illumination of the object at grazing angles of incidence from inside the microsphere. It takes place non-resonantly which makes it unrelated to the resonant WGM excitation. Such circulating modes were previously studied due to near-field coupling between different microspheres [23]. Therefore, this work creates a big opening for new theoretical studies that will be used by experimental physicists for different microspheres and different geometrical shapes of objects.

Experimental findings have showcased the feasibility of achieving super-resolution imaging through microspheres when submerged in a liquid medium with an index exceeding 1.9. Specifically, barium titanate glass (BTG) microspheres, characterized optically in an aqueous environment, exhibit indices ranging approximately from 1.9 to 2.1 [87,88]. Utilizing micron-scale BTG microspheres immersed in isopropyl alcohol (IPA) with an index of 1.37, researchers

have successfully discerned features as minuscule as approximately λ/7, where λ = 550 nm represents the peak illumination wavelength. The process of virtual image formation is depicted in Figs. 2(a) and 2(b). For spheres measuring between 50 μm and 200 μm in diameter, the distinguishable feature sizes expand to approximately λ/4. Moreover, the super-resolution field-of-view exhibits a linear increase in diameter, attaining remarkably large dimensions, approximately 30 μm, for spheres around 200 μm in size. The magnification of the virtual images falls within the range of 2.5 to 4.5 for spheres ranging in diameter from 2 μm to 220 μm.

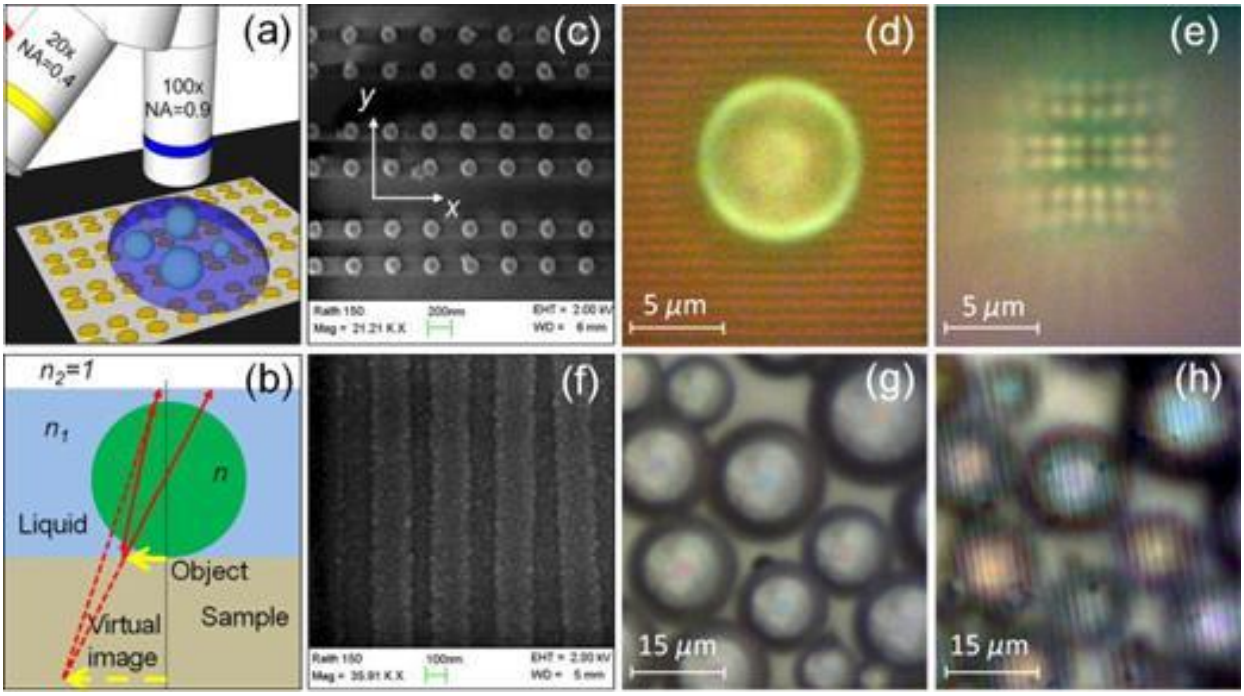

Figure 2: Virtual Image of gold dimers and Blu-ray disc. (a) Illustration of the experimental arrangement; (b) Representation of virtual image formation using a sphere immersed in liquid; (c) Scanning electron microscope (SEM) depiction of a collection of gold dimers formed by 120 nm nanoparticles with separations of 150 nm; (d) BTG sphere with a refractive index approximately 1.9, submerged in isopropyl alcohol (IPA); (e) Virtual imaging of the array depicted in (c) through the microsphere at an alternative depth compared to (d) using a 100× objective with a numerical aperture (NA) of 0.9; (f) SEM image showcasing a Blu-ray disk featuring stripes of 200 nm width separated by 100 nm width grooves; (g) BTG microspheres with diameters ranging approximately from 5 to 20 μm, fully immersed in IPA; and (h) Virtual imaging of the Blu-ray disk through the microspheres at a different depth compared to (g) using a 20× objective with a numerical aperture (NA) of 0.4 [105].

The samples containing point objects, as depicted in Fig. 2(c), comprised 2D arrays of gold nanoparticle dimers with periods of 320 nm and 800 nm in the *x* and *y* directions. Each dimer comprised two gold nanocylinders with diameters of 120 nm and heights of 30 nm (including 2 nm Cr and 28 nm Au layers), fabricated on a fused silica substrate through electron beam lithography, metal evaporation, and lift-off processes. The smallest edge-to-edge separations within the dimers measured 120 nm and 150 nm in distinct arrays. The SEM image featured in Fig. 2(c) illustrates NPDs with a 150 nm separation along the y direction. Samples featuring linear objects were derived from a commercially available Blu-ray® disk (BD) with track pitch sizes nominally set at 300 nm, comprising 200 nm width stripes separated by 100 nm width grooves, as outlined in Fig. 2(f). Two variations of BTG microspheres (Mo-Sci Corp.), distinguished by their chemical composition and hence their refractive index (approximately 1.9 and 2.1), were utilized. IPA was administered onto the sample surface using a micro-syringe to completely submerge the microspheres. Comparable outcomes were achieved through water infiltration.

The study utilized an FS70 Mitutoyo microscope with a halogen lamp and CCD camera, operating in reflection illumination mode with either 100× (NA = 0.9) or 20× (NA = 0.4) microscope objectives. The system's spectral response peaked strongly at 550 nm, and by employing additional filters, ensured reproducible results with narrow band (~20 nm bandwidth) illumination centered at 550 nm. Conventional microscopy failed to resolve the smaller features within the samples, such as the 320 nm period and 150 nm edge-to-edge separations in NPDs, as well as the 100 nm features in the BD, due to limitations imposed by the stripe pattern outside the microsphere. Super-resolution imaging of the BD without liquid was achievable using

microspheres with small-to-moderate refractive indices, such as borosilicate glass (n ~ 1.47), soda lime glass (~1.51), polystyrene (~1.59), and sapphire (~1.77). However, complete immersion in a liquid like IPA caused these microspheres to lose their imaging capabilities entirely. A different behavior was observed for high-index BTG spheres (with n ~ 1.9-2.1). They didn't produce any imaging without the addition of liquid, but when fully submerged, they enabled super-resolution imaging, exemplified in Figs. 2(e) and 2(h) for point and linear objects, respectively. Notably, the depth of focus in these images was observed below the structure's surface, discernible from conventional images Figs. 2(d) and 2(g). The ability to resolve individual gold nanoparticles and features on a BD, both approximately λ/4 in size, was evident. Despite the complexity of applying the Rayleigh criterion due to finite object sizes, discerning patterns with such minimum feature sizes were achieved.

Furthermore, in prior studies, the field-of-view (FOV) was limited to a few microns due to the small diameters of low-index spheres [89-91]. However, high-index liquid-immersed spheres maintained their super-resolution capability even at significantly larger diameters. For instance, a sphere with n ~ 1.9 and D ~ 125 μm resolved 150 nm separations in an NPD array over large (~22 μm) FOV, as illustrated in Figs. 2(a) and 2(b). Similar outcomes were observed for the BD sample using a sphere with n ~ 2.1 and D ~ 53 μm fully immersed in IPA, depicted in Figs. 3(c) and 3(d).

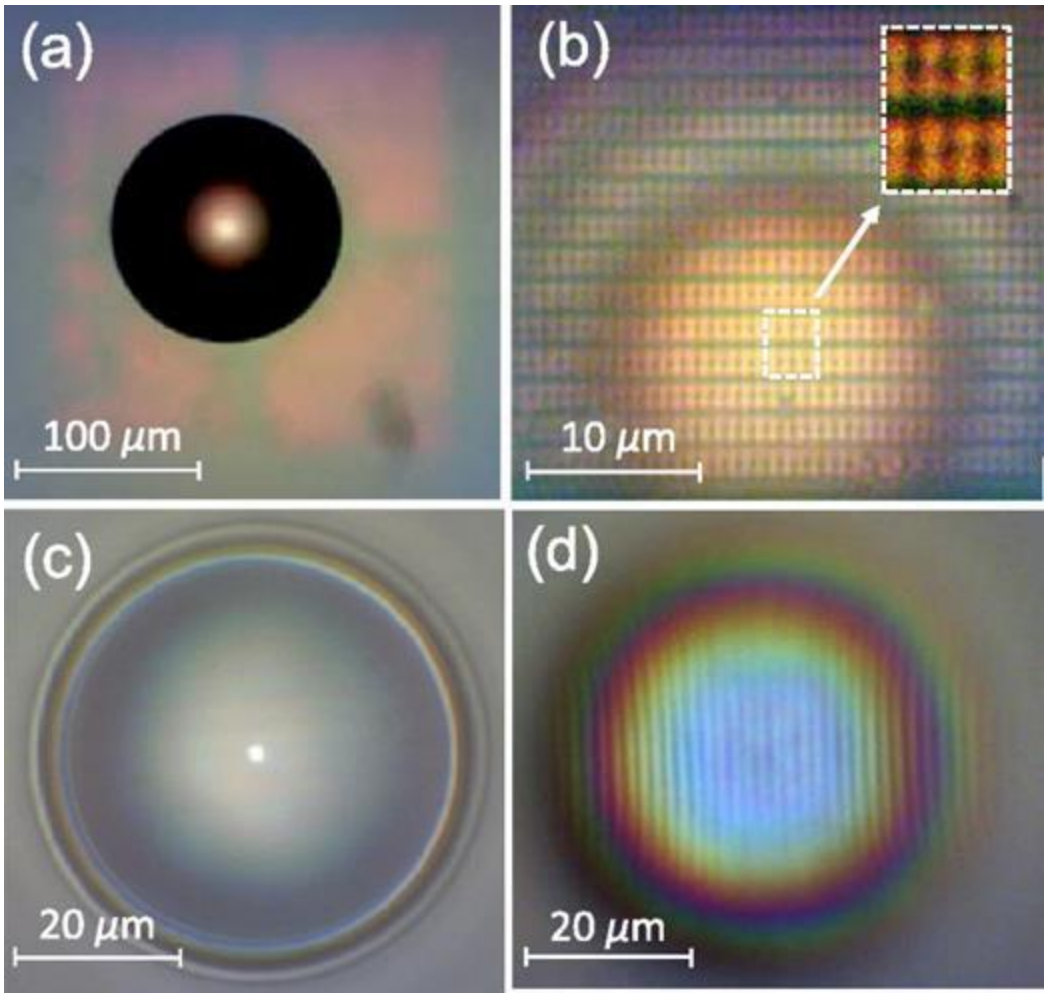

Figure 3: Nanoparticle dimers resolved by high-index spheres. (a) A BTG microsphere with a refractive index of approximately 1.9 and a diameter around 125 μm, completely submerged in IPA, positioned atop the NPD array featuring 150 nm separations. (b) Illustration of imaging through this microsphere using a 100× objective lens (NA = 0.9), showcasing a super-resolution field-of-view exceeding 20 μm. (c) A BTG microsphere with a refractive index of approximately 2.1 and a diameter of around 53 μm, fully immersed in IPA, situated atop a BD. (d) Depiction of imaging through this microsphere using a 20× objective lens (NA = 0.4), reveals the presence of 100 nm grooves on the BD [105].

In the investigation of the resolution capability's dependency on D, an NPD array featuring a minimal separation of 120 nm was utilized, as depicted in Fig. 4(a). It was observed that the resolution generally declined with increasing D, a trend demonstrated in Figures 4(b)–4(d). Intensity profiles were assessed along the axis connecting two nanoparticles with a 120 nm separation, as indicated in the insets of Figures 4(b)–4(d). These profiles exhibited double peak

structures, which were subjected to fitting using two Gaussian peaks. The sums of these Gaussian peaks were depicted by dashed (red) curves in Figures 4(b)–4(d). Specifically, for spheres measuring 4.2 μm in diameter, the minimal discernible feature sizes were estimated to be around 75 nm (~λ/7), considering that two equally intense points are resolved when the intensity between them is 0.81. Conversely, for spheres with D = 53 μm, adhering to the same criterion led to minimal discernible feature sizes of approximately λ/4.5.

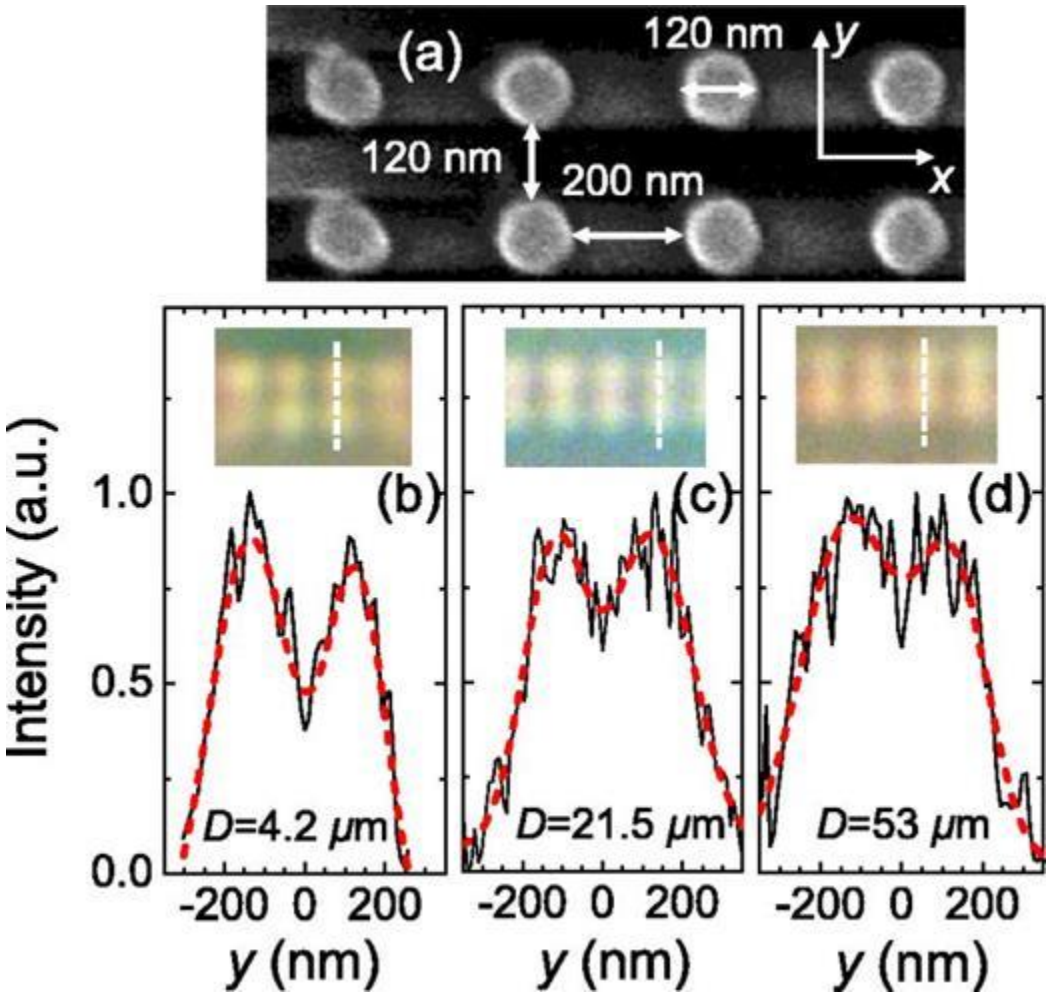

Figure 4: Resolution quantification of nanoparticle dimers. (a) Scanning electron microscope (SEM) depiction of a gold nanoparticle dimer (NPD) array formed by 120 nm nanoparticles with separations of 120 nm, alongside the resolution capabilities of BTG microspheres with a refractive index around 1.9 and various diameters D: (b) -4.2 μm, (c) -21.5 μm, and (d) -53 μm.

Insets exhibit the optical microscope images acquired for the (b)–(d) scenarios, corresponding to the SEM image in (a) [122].

In examining image magnification (M), microspheres with refractive indices around 1.9 and diameters ranging from 2 to 220 μm were used, as depicted in Figure 5(a). The refraction law, determined by the index contrast ($n' = n/n1 \sim 1.39$), allowed estimation of virtual image magnification for objects situated at the sphere surface, approximately $|M| \sim |n'/(2 - n')| \sim 2.3$. For spheres with diameters around 220 μm, a measured M of approximately 2.5 was obtained. Conversely, for the smallest spheres ($2 < D < 6$ μm), increasing M with sphere diameter was observed, mirroring findings from previous studies involving low-index spheres in air. In the intermediate diameter range ($6 < D < 10$ μm), M peaked at values ranging from 3.5 to 4.5, with significant variations observed among spheres, as illustrated in Figure 5(a).

However, the measurement of M was challenging due to difficulties in reproducing the same depth of focus on the virtual image. Additionally, pincushion distortion caused an increase in image magnification with distance from the optical axis, as evidenced in Figure 1(e) and the inset of Figure 5(b). To mitigate the pincushion effect, M was determined in the central image section. The field-of-view (FOV) was defined as the diameter of the circle on the sample surface where the shape of the NPD array with 150 nm separations could be discerned, showing a close-to-linear dependence on D, as depicted in Figure 5(b).

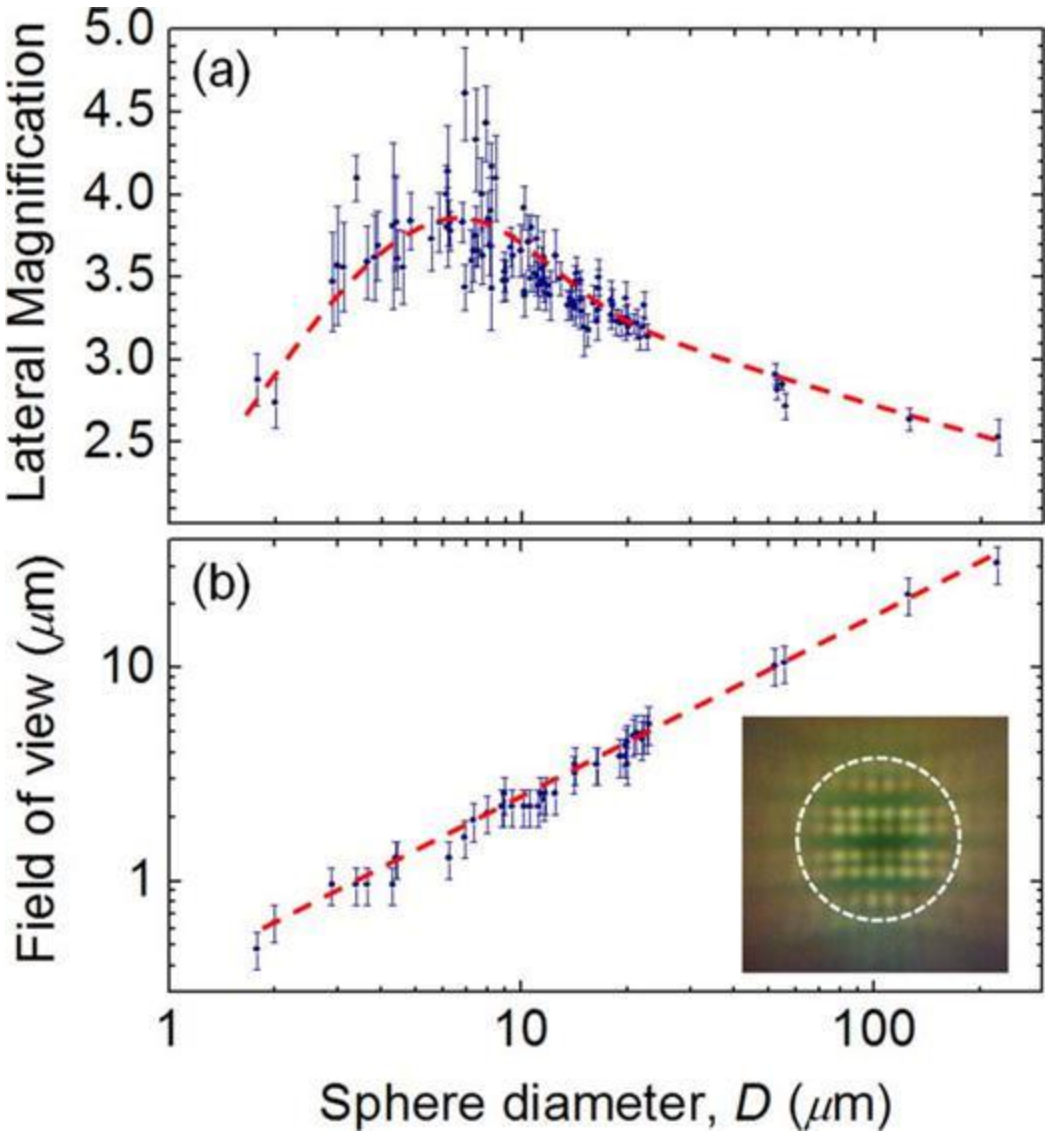

Figure 5: Relationship between sphere diameter, field of view, and magnification. (a) Lateral magnification and (b) Field of View (FOV) achieved by BTG microspheres with a refractive index of approximately 1.9, plotted against D. The inset in (b) demonstrates the FOV for a sphere with a diameter of 9 μm. These measurements were conducted utilizing the NPD array. Dashed lines have been included as visual aids for interpretation [122].

The study showcased the capability of discerning patterns with minimum feature sizes of approximately λ/7 using BTG microspheres (n ~ 1.9–2.1) with diameters in the range of several microns. As the microsphere diameters increased within the range of $50 < D < 220$ μm, the discernible feature sizes also increased to approximately $\lambda/4$. Moreover, it was noted that the

super-resolution Field of View (FOV) exhibited a linear correlation with *D*, with FOV values surpassing 30 μm for microsphere diameters exceeding 200 μm.

Despite the fact Field of View (FOV) exhibited a linear correlation with *D*, it remains a problem in MAMs. This problem can be solved by different techniques such as translations of the microsphere followed by stitching the images or by assembly of large-scale arrays of microspheres embedded in coverslips allowing parallel imaging through multiple microspheres. In the pursuit of developing an optimal method for assembling and fabricating an array of microspheres embedded in a coverslip, meticulous experimentation and analysis were used [24-30]. The objective was to refine the assembly process to achieve optimal performance and structural integrity. By systematically evaluating various fabrication techniques, the goal was to enhance the overall efficiency and reliability of the microsphere array for subsequent applications. It should be noted that quasi-periodic arrays of microspheres embedded in coverslips can also behave similarly to diffraction gratings or photonic crystal waveguides [31-33]. In the case of sufficiently large microspheres, however, these properties are not pronounced, and they lie outside the scope of this work.

1.3. Cellphone-based microscopy

The emergence of cellphones equipped with advanced imaging capabilities has stimulated interest in cellphone-based microscopy as a means for rapid disease identification without the need for traditional microscopes and their bulky apparatus [34-37]. The resolution of conventional cellphone cameras is constrained at approximately 20-40 μm level by the finite size of the pixels in the sensor array. The underlying problem of using conventional cellphone

cameras as portable microscopes is connected with insufficient image magnification provided by the camera objective in comparison with the high-quality microscope objective designed for maximizing *M* and NA values. The way of solving this problem is connected either with bringing the investigated sample in direct contact with the camera's sensor array or with using micro-optics to additionally magnify the image. Another solution is based on using lens-free holographic approaches, such as those utilized by Ozcan et al., demonstrating high resolution across expansive fields albeit requiring the removal of the camera lens and numerical reconstruction of images [37,38].

To address this limitation, additional magnifying objectives like ball lenses have been employed in such applications as the diagnosis of iron deficiency and sickle cell anemia in a blood smear [38], detection of soil helminths in stool samples [39], male infertility screening [40], and identification of malaria parasites [41], but typically with rather much-limited magnifications. Yet, ball lenses exhibit significant spherical aberrations leading to image distortion across the field-of-view, necessitating image capture at varying focusing depths and subsequent digital image processing [93]. Prior efforts in this realm employed ball lenses positioned at millimeter-scale distances from objects to generate real images, presenting a tradeoff between resolution and field-of-view It improved the resolution compared to conventional cellphone imaging up to approximately 1.5 μm values However, further increase of magnification is needed to improve the resolution beyond this level still determined by the pixelation effects.

In this study, a somewhat different approach to cellphone microscopy is proposed, involving the utilization of large ball lenses placed in direct contact with the samples, which can be translated over objects' surface. This configuration was inspired by the recent successes of MAM techniques where the resolution beyond the classical diffraction limit was demonstrated experimentally using high-quality microscope objectives [97–108]. Research has demonstrated the attainment of resolutions approaching λ/7 for imaging nanoplasmonic structures, and similarly, high resolutions have been achieved for imaging fluorescent objects coupled to plasmonic meta-surfaces with short periods. These resolutions surpass the limits of both microscope objectives and solid immersion lenses [109-111]. In cellphone-based applications, the high-resolution capabilities of such lenses are attributed to the magnification of virtual images. However, FoV was rather limited in the previous studies performed with small microspheres (typically D<10 μm) and showed some advantage in resolution studies, but the use of such compact microspheres inevitably narrowed FoV.

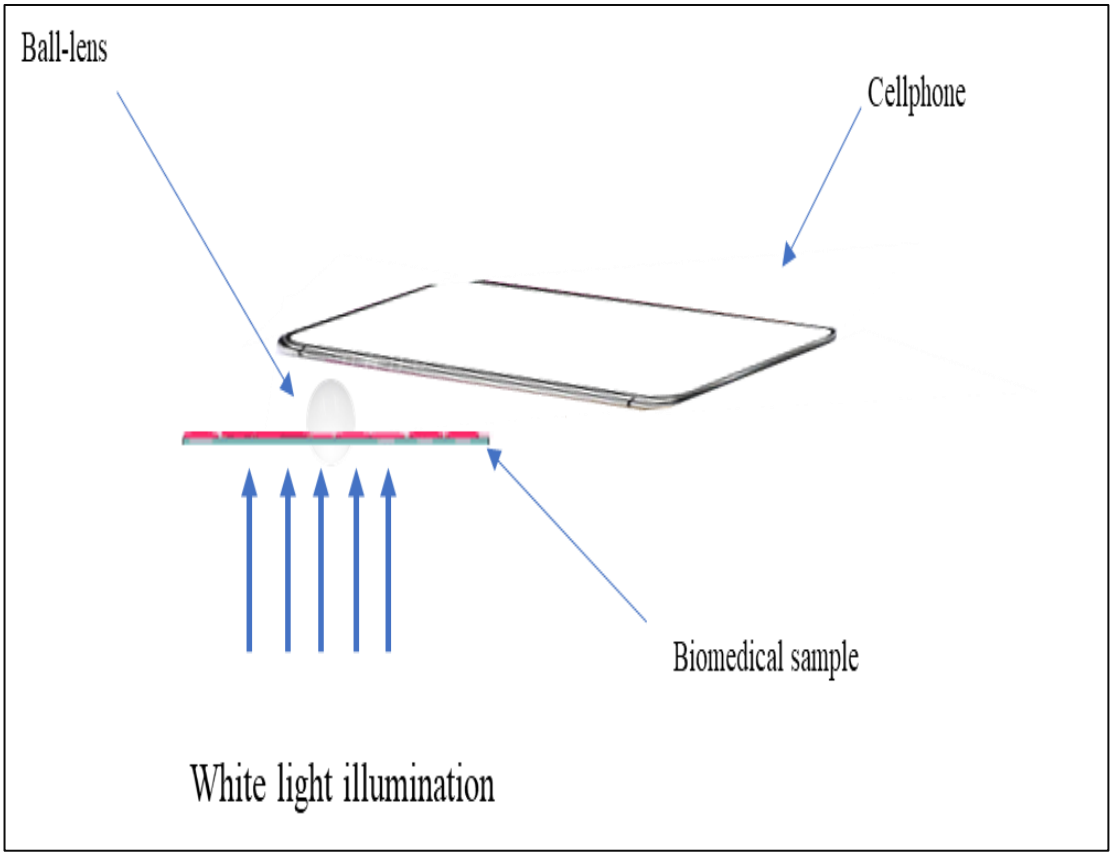

Figure 6: Cellphone-based microscopy setup.

CHAPTER 2: FABRICATION OF ARRAY OF MICROSPHERES EMBEDDED IN COVERSLIP

2.1. Previous work on microspheres embedded in polydimethylsiloxane (PDMS).

Since the groundbreaking utilization of millimeter-sized glass microspheres by Van Leeuwenhoek for early microscopy in 1675, the trajectory of microsphere-assisted microscopy has seen a resurgence, with significant advancements documented in recent times, notably in 2011 [112]. The fundamental premise of this technique revolves around the strategic placement of small glass microspheres, typically ranging from 5 μm to 50 μm in diameter, onto the sample in front of the objective lens. This placement serves to substantially augment the resolution capabilities of an otherwise conventional optical microscope. As researchers delve deeper into refining this methodology, various ingenious approaches have emerged to optimize the assembly of microspheres, thus expanding the field of view attainable through this technique. Among the myriad strategies devised to enhance the effectiveness of microsphere-assisted microscopy, one advancement hails from the Mesophotonics lab at the University of North Carolina, directed by Professor Vasily Astratov. This innovative approach involves the integration of microspheres within a matrix of polydimethylsiloxane (PDMS). Upon the solidification of the PDMS composite with embedded microspheres, the resulting construct can be delicately affixed onto the surface of the specimen under investigation. Close contact with the object is critical for microspheres embedded in the coverslip to provide resolution enhancement. This means that the gap separating the microspheres from the object should be minimized. This can be achieved in two different ways. Firstly, the freshly fabricated PDMS coverslip with microspheres embedded near one of its surfaces is attached to a semiconductor, glass, or plasmonic substrate with a flat object. Similar to the Geico toy, the PDMS slab gets closely attached to the substrate which can

be monitored by observation of the motion of interference stripes indicating a gradual reduction of the gap. In the second way, liquid lubrication can be used to initially fill this gap with the thin liquid layer. Gradual liquid evaporation leads to a reduction of this gap, which can be also monitored by observation of the motion of interference fringes. An additional advantage of the second technique is the ability to shift the coverslip to provide the best conditions for the observation of objects through embedded microspheres. Subsequently, through meticulous mechanical manipulation, facilitated by lateral translation, the embedded microspheres can be precisely aligned with the regions of interest within the specimen. Experimental endeavors undertaken to validate the efficacy of this methodology have elucidated the critical role of surface lubrication with isopropanol (IPA) in facilitating the smooth lateral translation of matrices harboring embedded spheres.

In the experimental setup depicted in Figure 7(a), a diverse array of high-index barium titanate glass (BTG) microspheres, exhibiting a range of diameters spanning from 9 to 212 μm, was meticulously deposited onto a substrate. It's noteworthy that two distinct categories of BTG spheres, each characterized by unique refractive indices of 1.9 and 2.1, respectively, were selected for this experiment, thus adding a layer of complexity and nuance to the experimental framework. Subsequently, a polydimethylsiloxane (PDMS) layer was cast over the array of BTG spheres, as illustrated in Figure 7(b). The encapsulation process was further refined through thermal treatment within a temperature-controlled oven, ensuring the uniform curing of the PDMS layer to attain optimal results. Upon the completion of the thermal curing process, the resultant thin film, now transformed into an elastomeric state, underwent a delicate extraction process from the substrate. It involved the deft manipulation of a scalpel to carefully lift the PDMS layer, liberating it from its substrate confinement, as depicted in Figure 7(c).

The thin film was scanned across the investigated surface, revealing its topography with remarkable clarity. To visualize the surface, two imaging systems were used. Firstly, the FS70 Mitutoyo microscope in a reflection mode with the halogen lamp emission peaked at λ ~550 nm, complemented by a CMOS camera. Secondly, the scanning laser confocal microscope Olympus LEXT OLS4000, operating at λ = 405nm. The virtual images were obtained through BTG microspheres. Figures 7(d) and 7(e) showcase the high-index microspheres embedded in PDSM. Within these images, the depth of focus was around the equator plane of spheres. The ability to seamlessly translate the entire thin-film along the surface simplified the alignment process of diverse spheres with the object of study.

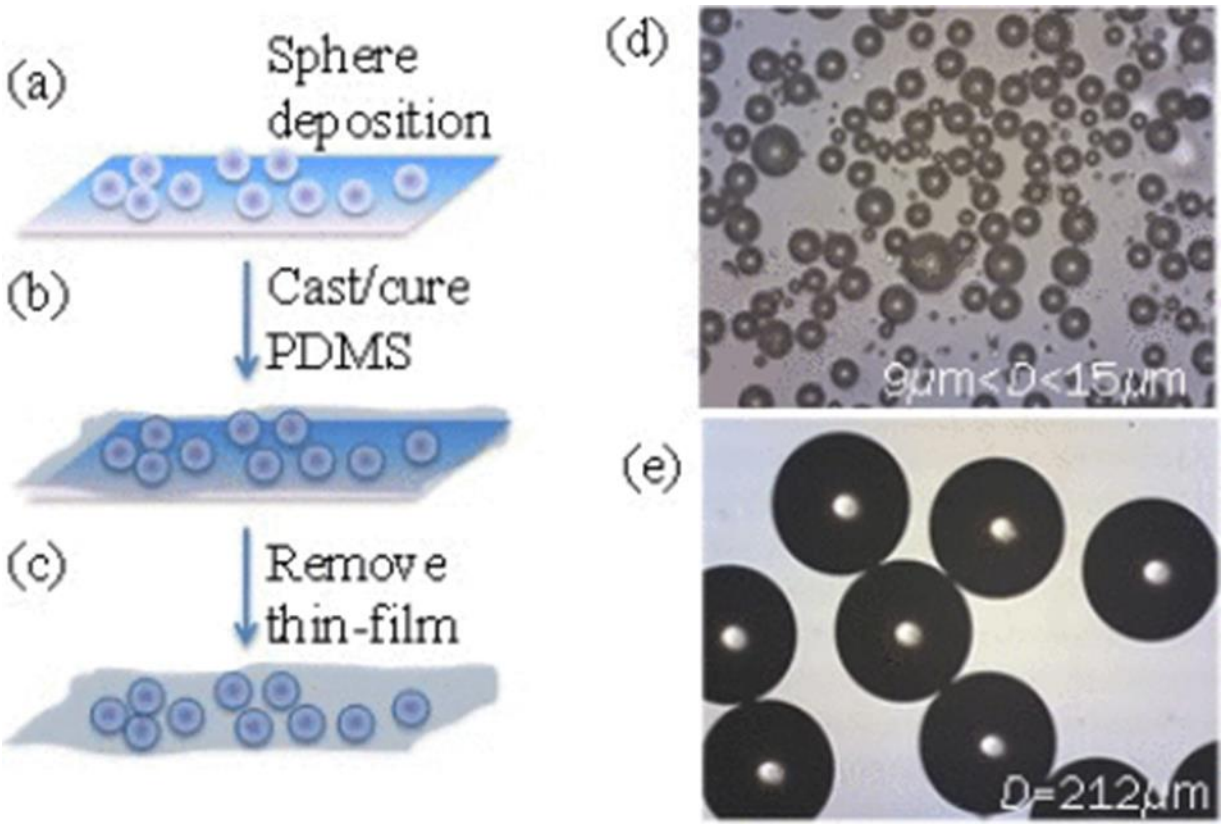

Figure 7: Fabricating transparent PDMS matrices. (a-c) Depiction of the intricate process involved in fabricating transparent PDMS matrices featuring embedded high-index spheres. (d) An optical microscope capture showcasing BTG spheres with diameters ranging from 9 to 15 μm securely embedded within a PDMS matrix. (e) Another optical microscope image reveals BTG spheres with a substantial diameter of 212 μm ensconced within a PDMS matrix [112].

Nanoplasmonic arrays of dimers, fabricated by e-beam lithography served as the focal point of this experimental investigation. The investigation was focused on dimers characterized by a diameter of 175 nm and a center-to-center distance of 200 nm, resulting in an ultrafine 25 nm separation, a mere fraction of the incident wavelength (~λ/16), as demonstrated by the SEM image in Fig. 8(a). The Au layer with 40 nm thickness was deposited on top of the 10 nm thick titanium adhesion layer. The dimers were defined by the electron beam lithography.

The visual examination of these nanoplasmonic arrays was facilitated by a ~13 μm BTG sphere embedded in PDMS, enabling imaging via a scanning laser confocal microscope equipped with a high-powered 100× objective boasting a numerical aperture (NA) of 0.95 at λ=405 nm laser illumination, as depicted in Fig. 8(c). To quantify the resolution of the captured images, a rigorous analysis was undertaken utilizing the convolution with the point spread function (PSF) of the imaging system. Fig. 8(d) visually represents the result of such a convolution process for the optimized width of the Gaussian PSFs for comparison with the experimental image. Thus, a good agreement between the calculated (Fig. 8(d)) and experimental (Fig. 8(b)) was realized for the PSF width about λ/7.

Following Houston's criterion, the width of the PSF~λ/7 was taken as the de facto measure of resolution.

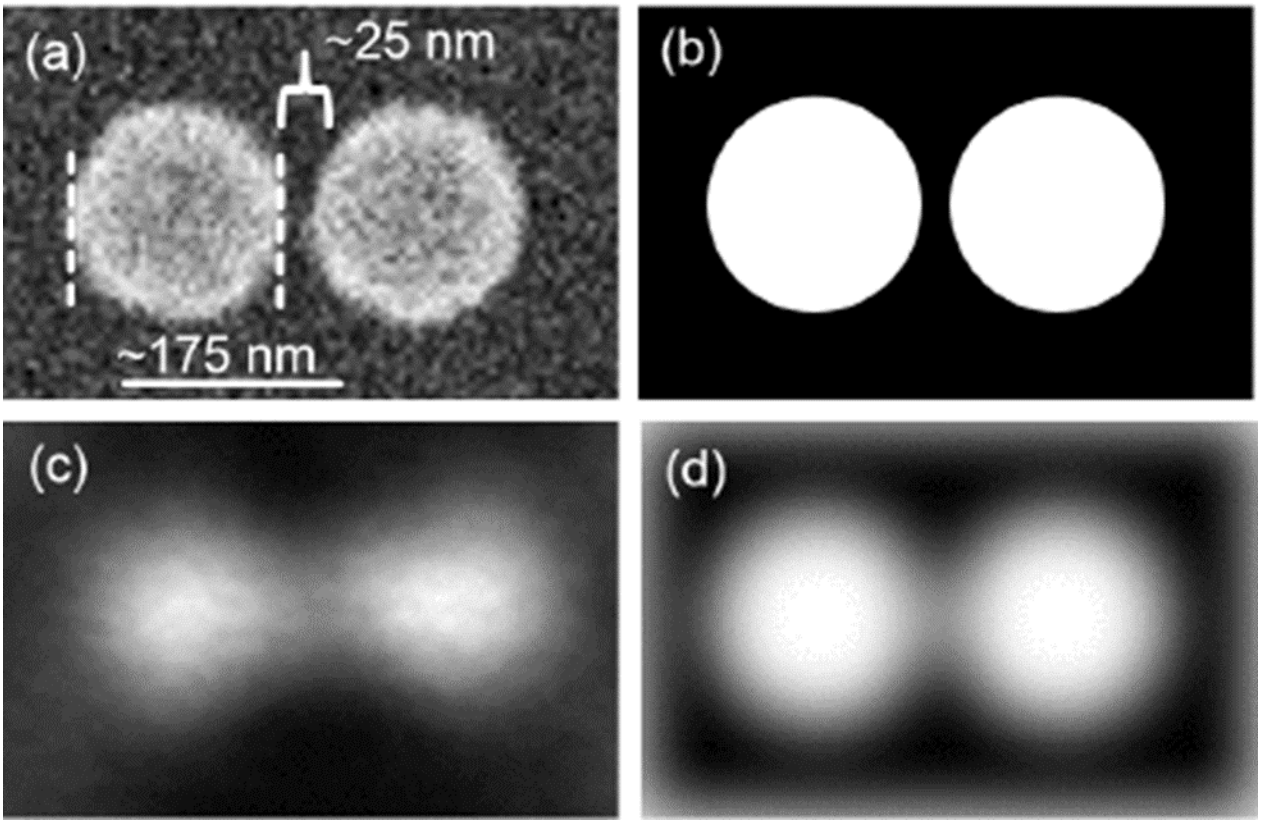

Figure 8: Image of the gold nanoplasmonic dimer. (a) An image captured by a scanning electron microscope showcasing the gold nanoplasmonic dimer. (b) A visual representation of the object is utilized for computing a convoluted image. (c) The visual depiction of the dimer was acquired through the utilization of a microsphere embedded within the PDMS thin-film. (d) A computed image illustrating the convolution process between the drawn object in (b) and a point spread function characterized by a width of approximately λ/7 [112].

2.2. Fabrication process

The viewing capacity of the microsphere super-lens is constrained by its size and the distortions present at the boundary of FoV. As the diameter of the super-lens increases, the FOV expands proportionally; however, this expansion is accompanied by a decline in resolution. This restricted FoV imposes limitations on practical applications, prompting the exploration of alternative methods such as probe-based manipulations [28,118] and embedding microspheres into elastomers [25-31] to enable observations from predetermined positions. These approaches, however, encounter

challenges in achieving expansive imaging coverage and precisely pinpointing sub-diffraction-limited targets across extensive areas.

To solve this issue and to apply this technology in a cellphone-based setting, it is desirable to increase the size of the microspheres embedded within plastic coverslips. According to a conventional definition, microspheres with diameters larger than 100 μm are termed the ball lenses. We use this terminology in the following parts of this thesis. Such ball lenses can provide a somewhat reduced resolution compared to mesoscale (D<10 μm) microspheres. However, they are more suitable for integration with the cellphone camera due to their larger FoV.

Another problem appears with the integration of such ball lenses into sizable arrays. Biomedical samples have millimeter and, in some cases, centimeter-scale dimensions. This means that hundreds of ball lenses need to be arranged in regular arrays. It is also desirable to provide a maximal area fill-factor with the ball lenses to have a good coverage of the surface of the sample. The maximal area fill-factors can be achieved in regular close-packed arrays of ball lenses. However, assembling hundreds of ball lenses in regular arrays is not a simple task. Relying on self-assembly does not work very well for such assembly since it can lead to the formation of isolated clusters of ball lenses or domains with different types of packing ball lenses. It could also lead to a certain concentration of local defects which is an inevitable property of self-assembly. All these problems would spoil the quality of imaging by such arrays.

To solve this assembly problem, we used a technology that was previously developed in the Mesophotonics Laboratory directed by Prof. Astratov for arranging spherical microlenses in an orderly way suitable for integration with the mid-wave infrared (MWIR) photodetector focal plane arrays (FPAs) [42-47]. This technology is based on the fabrication of micro-hole arrays with the desired geometrical properties such as square or triangular perfectly ordered arrays obtained by well-

established technology such as micromechanical drilling of holes in metallic thin films or etching micro-holes in a thin semiconductor substrate. The holes must extend through the entire thickness of the corresponding metallic film or semiconductor substrate. The assembly of microspheres is achieved in this method by air flux provided through micro-holes. The principle of assembly reminds operation of suction tweezers. However, in contrast to suction tweezers manipulating individual items, the suction assembly in a micro-hole array allows obtaining a large-scale array with hundreds of ball lenses, each one sitting in a separate micro-hole, forming a perfectly ordered pattern with virtually zero concentration of defects such as missing ball lenses, and very large area fill-factor. The ball lenses can be assembled in practically touching configuration. This method represents an example of forced or deterministic assembly as opposed to self-assembly and this is the underlying reason for the nearly perfect order of thus obtained arrays. Airflow through individual micro-holes attracts the nearest microsphere which is kept at a fixed position once the flux persists. As a result of a prolonged process, all micro-holes will be filled with the ball lenses, allowing approximately half of each microsphere to nestle snugly within the confines of the holes. This procedure ensured a uniform and orderly arrangement of the microspheres.

To further refine the arrangement and eliminate any interstitial ball lenses that can be located on top of the assembled monolayer of lenses, pressurized air was judiciously employed to sweep away any balls or pieces of dust that might have accumulated. This step needs to be designed with the continuous flux through the micro-holes which kept the balls fixed in micro-holes in a correct pre-designed position, so that the additional sideway flux of air will simply clean the array from any additional ball lenses. Subsequently, with utmost care and precision, the coverslip was gently lowered onto the array of microspheres located within the micro-holes.

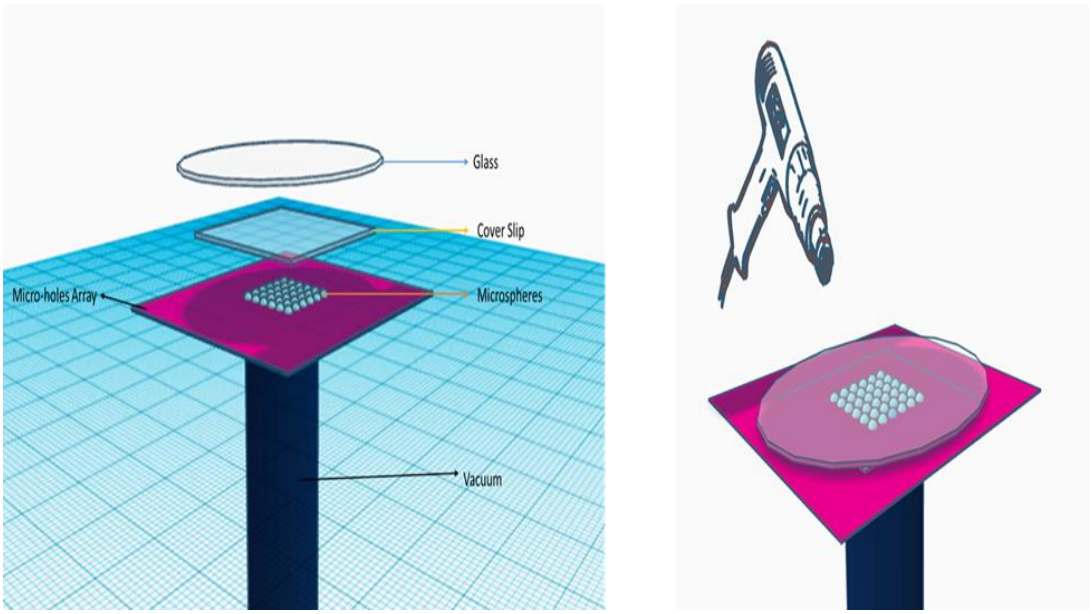

Figure 9: The assembly process of the microsphere array.

Once the coverslip was in place, the entire assembly underwent a controlled heating process facilitated by a heat gun, as illustrated in Fig. 9. The application of heat served the dual purpose of partially fusing the microspheres to the coverslip while maintaining their structural integrity. This step was important for securing the microspheres in their designated positions, ensuring they remained firmly attached to the coverslip. Following the heating process, the partially adhered microspheres were transferred to a thermal press, where they underwent further embedding in the plastic coverslip. Previously, the technique of pressure embedding much smaller microspheres (D~5-50 μm) in plastic coverslips was used for making slabs for super-resolution imaging of plasmonic and biomedical structures [29, 48,49,50,51,52]. In this thesis work, we decided to develop similar methods for embedding much larger ball lenses with diameters 100-1000 μm more suitable for applications in cellphone-based microscopy.

Under controlled conditions, the assembly was subjected to temperatures reaching approximately 185 degrees for a duration of five minutes under controllable pressure conditions

provided by the thermal press illustrated in Fig. 10. This combination of temperature and time allowed for optimal embedding of ball lenses in plastic coverslip, ensuring a durable and stable bond. This fabrication process yielded coverslips with relatively well-ordered ball lenses firmly attached to the coverslip and slightly extending from it as schematically illustrated in Fig. 10. The height of extending ball lenses was reasonably uniform due to the fact that the ball lenses were pressed against perfectly polished flat slab of the glass.

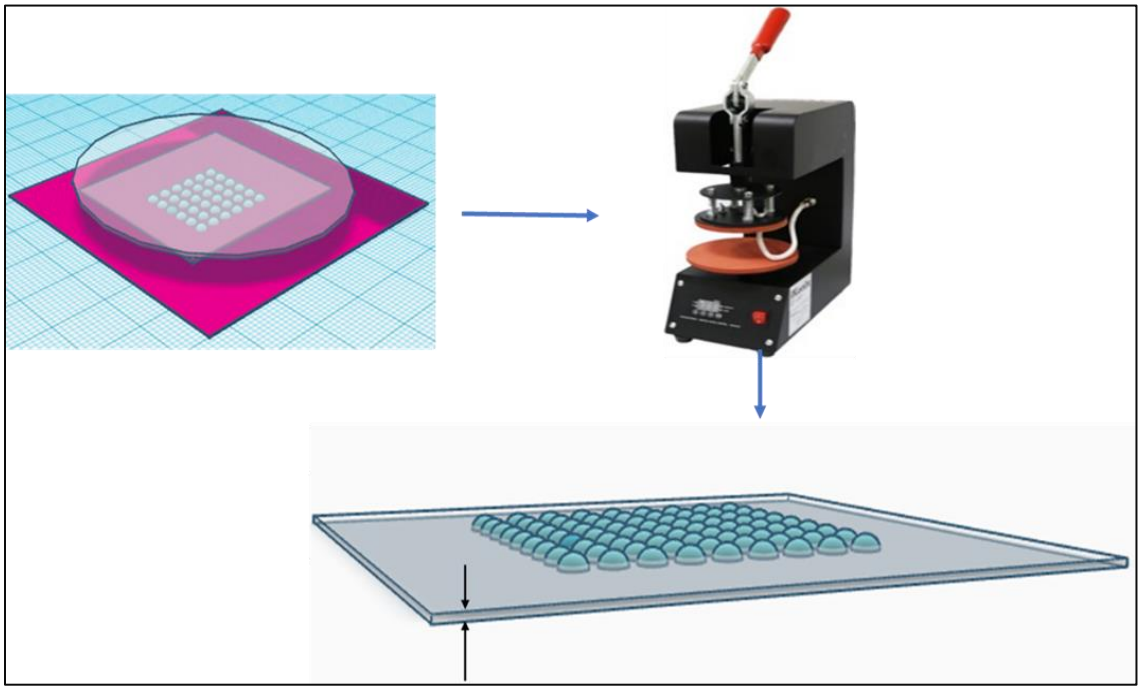

Figure 10: Fabrication process of the microspheres embedded in the coverslip.

The results of such an assembly are illustrated in Figure 11. The ball lenses used in Figure 11(a) are BTG with an index of 2.1 and a diameter of 300 μm. The ball lenses used in Figure 11(b) are BTG with an index of 2.1 and a diameter of 550 μm. The comparison of these images demonstrates that the method of suction assembly works considerably better for larger ball lenses. Indeed, the quality of ordering embedded ball lenses is rather reasonable although not perfect. Whereas the results for ball lenses with diameters smaller than 300 μm demonstrated

multiple defects and lack of perfect order. There might be different reasons for the lack of ordering including the deviation of the ball lens sizes (typically within ~5%) and the increased role of the other forces besides the suction action. Assembly of smaller spheres is more prone to charging effects, as an example. This does not mean that the suction assembly cannot be used for ball lenses with D<300 μm. Based on our preliminary results, we believe that a much better quality of assembly can be obtained in future work. It can be achieved by removing charging effects using surface chemistry or by controlling the process of mechanical assembly. As an example, a slight shake of the micro-hole array provided by mechanical actuators can help to obtain better-ordered arrays formed by the ball lenses with *D*<300 μm. These studies can be performed in future work.

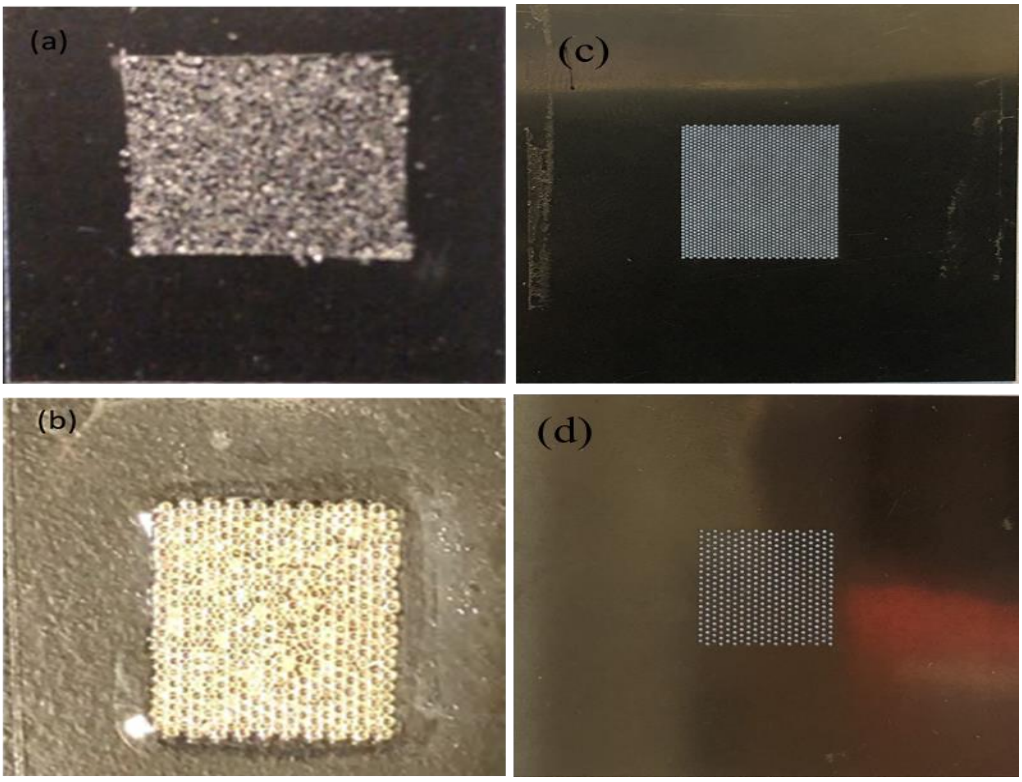

Figure 11: Fabrication process of the microspheres embedded in the coverslip. (a) Array of microspheres with a diameter of 300 micrometers. (b) Image of microspheres with a diameter of 550 micrometers embedded in plastic coverslip. (c) Micro-hole arrays with a diameter of 305 micrometers fabricated by laser burning. (d) Micro-hole arrays with a diameter of 600 micrometers fabricated by laser burning.

2.3. Real and Virtual Imaging Illustrations

In 2011, Wang et al. [115] discovered the superior resolution capabilities of microspheres compared to solid-immersion lenses (SIL) when placed near samples. They found that by placing microspheres on the sample, they could observe a virtual image through the silica microsphere, allowing them to resolve the minimal feature sizes as fine as 50 nm. These microspheres, with an index of refraction of n=1.46 and diameters ranging from 2 μm to 9 μm, functioned as far-field super-lenses (FSL), effectively overcoming the white-light diffraction limit. This initial work stimulated significant interest in this type of microscopy, however, at first the resolution claims were exaggerated reaching λ/8 -λ/14 (far-field resolution) with magnification values being between ×4 and ×8.

More rigorous resolution quantification can be performed by convolution with PSF and fitting the experimental intensity profiles obtained from various nanoscale objects using the width of PSF as a fitting parameter. Initially, this was performed using 1-D PSF [13], but soon after this technique was generalized for fitting images of the objects with arbitrary shapes using convolution with 2-D PSF [25-29]. Subsequent efforts have been dedicated to understanding the mechanism behind this phenomenon and improving resolution. Recent research has even shown the feasibility of utilizing high-refractive index microspheres to generate real super-resolved images [114].

The distinction between virtual and real imaging is illustrated in Fig. 12. It is illustrated in the case of cellphone imaging, but similar images can be observed by using a regular microscope camera with the sensor array. The difference between virtual and real imaging is

illustrated using ray optics. As shown in Fig. 12(a), the virtual image is located at the continuation of the rays below the sample surface in the case of upright microscopy. Experimentally, virtual imaging can be counterintuitive in some cases since the image can be located deeply inside the absorbing substrate. This, however, does not prevent us from observing the virtual image since it takes place due to ray tracing in the direction opposite to the direction of light propagation and light does not physically propagate inside the absorbing substrate. Understandably, virtual imaging takes place if the refraction capability of the ball lens is limited. The case in Fig. 12(a) is illustrated for the index of the ball lens with n=1.52 corresponding to the index of borosilicate glass. Generally, most of the results obtained using the MAM method correspond to the virtual imaging case.

In contrast, the real image is located above the sample in the case of upright microscopy. It takes place due to the intersection of rays along their propagation direction (upwards). The real imaging case in Fig. 12(b) requires stronger refraction capability. This sketch illustrates schematically the refraction of rays by the ball lens with an index n=2.05. Such refractive indices are characteristic for barium titanate glasses as well as for LASFN 35 glass and for other high-index glasses. The real imaging by microspheres has been observed experimentally [53].

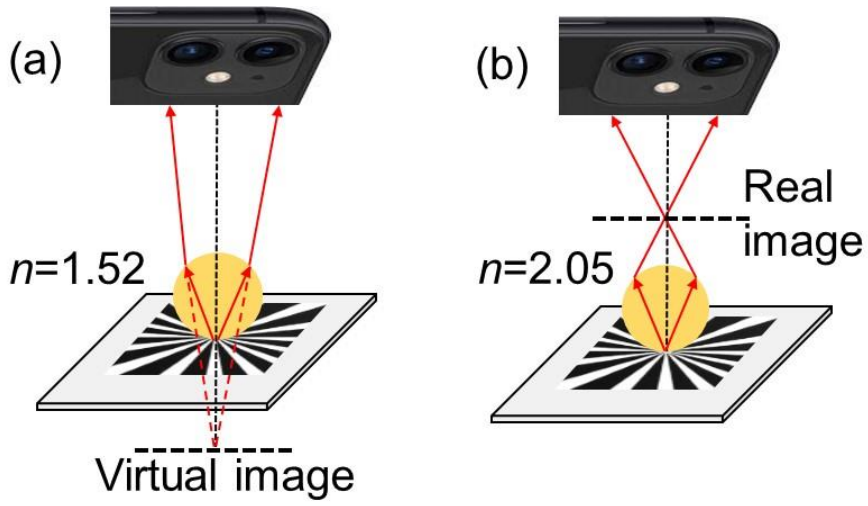

Figure 12: Ray tracing. Schematic illustration of the ray tracing in the case of (a) virtual and (b) real imaging. They take place at different refractive indices of the ball lens [55].

A more detailed description of contact imaging by ball lenses with different indices of refraction in the context of developing cellphone-based microscopy can be found in Refs. [54-58]. Wave optics-based theory of imaging by ball lenses can be found in Ref. [16]. We limit our discussion to the geometrical optics theory and concentrate mainly on the discussion of magnification provided by ball lenses with different indices of refraction as a function of separation between the ball lens and the object termed below as a gap (g). The equation describing magnification as a function of n and g to the best of our knowledge was first obtained in Refs. [26-28] in paraxial geometric optics approximation and widely used in the studies of nanoplasmontic and biomedical objects in the Mesophotonics laboratory directed by Prof. Astratov [59-73]:

$$M(n', D, g) = -n'/[n'-2+4(n'-1)g/D], \qquad (2)$$

where $n' = n/n_0$ is the refractive index contrast between the ball lens and object space with the refractive index n_0. In the following we follow the analysis presented in Ref. [55] and we consider the case of air environment where n_0 =1 and n'=n. This equation was used to calculate M values for the ball lenses with D=1 and 2 mm, as shown in Fig. 13. The gaps were varied in the $0 \leq g \leq 0.25$ mm range.

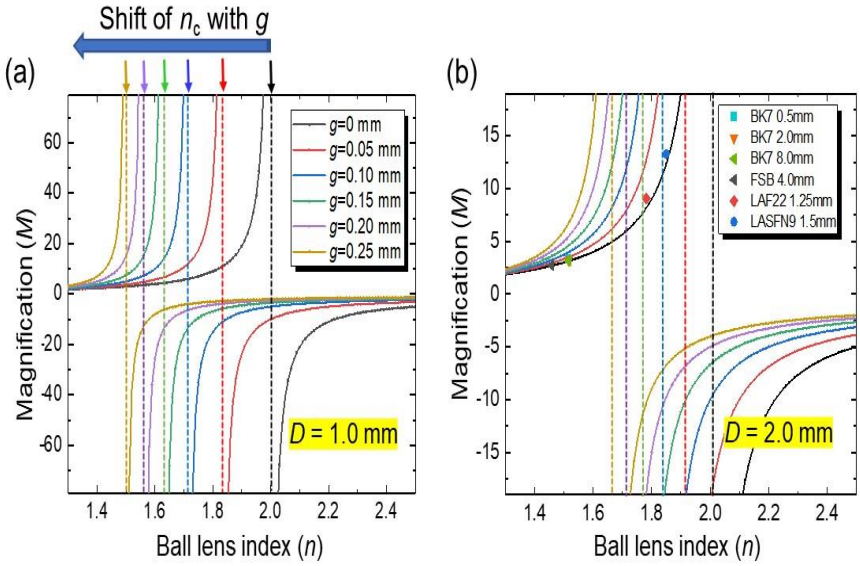

Figure 13: Geometrical optics results of solving Eq. (2) [55,56]. (a,b) Curves with different colors represent the magnifications of the ball lenses with D=1.0 and 2.0 mm, respectively, calculated as a function of n for various lens separations (g) shown in the legend of (a). Asymptotic increase of $|M|$ takes place at certain critical indices (n_c) indicated by vertical dashed lines. Virtual imaging corresponds to M>0 and real imaging corresponds to M<0. The points with different colors and shapes in (b) represent the experimentally measured M values for ball lenses made from different glasses in contact with the objects. The diameters and materials of the ball lenses are indicated in the legend of (b), where BK7 is a pure optical borosilicate-crown glass material with n=1.517 at λ=589.3 nm (the corresponding points for D=0.5, 2.0, and 8.0 mm coincide in (b)), FSB is a fused silica (quartz) balls with n=1.458 at λ=589.3 nm, LAF22 and LASFN9 are glasses with the refractive indices n=1.78 and 1.85 at λ=550 nm, respectively [55].

The most interesting and distinctive feature of Fig. 13 existence of a certain critical value (n_c) of the ball lens index, $n_c=(2g+D)/(2g+D/2)$, indicated in the case of D=1 mm by the vertical arrows on top of Fig. 13(a), which separates regimes of virtual and real imaging. In the case of virtual imaging $M>0$ since the image is located from the same side as the object relative to the optical axis, as illustrated in Fig. 12(a). On the other hand, in the case of real imaging $M<0$ since the image is located at the opposite side from the object relative to the optical axis, as illustrated in Fig. 12(b). In the vicinity of n_c an asymptotic increase of $|M|$ takes place that makes it possible to achieve very high magnification values in practical situations. Some of these situations realized with different microspheres made from glasses with different indices of refraction are illustrated in Fig. 13(b) under contact conditions (g=0) between the ball lens and object. Different materials used for comparing measured and calculated M values are listed in the legend of Fig. 13(b). This comparison illustrates good agreement between geometrical optics approximation and experiment for sufficiently large ball lenses. For a contact condition (g=0), n_c=2 for all D values. This is indicated by the black vertical lines in Figs. 13(a,b). However, with increasing g value, n_c gradually decreases and reaches value of n_c=1.5 for g=0.25 mm and D=1 mm. This shift of n_c with g is directly illustrated by the arrow at the top of Fig. 13(a). This shift is quite interesting since it shows that for many samples used in biomedical imaging studies where the objects are covered with glass coverslip with the typical thickness around g~0.1 mm, the value of n_c is actually smaller than two and it becomes closer to the indices of ball lenses made from more conventional glasses. The magnitude of this effect, however, depends on the diameter of ball lenses used in such studies. For smaller ball lenses the magnitude of shift increases which can be clearly seen by comparing results presented in Figs. 13(a) and 13(b) for ball lenses with diameters 1 and 2 mm, respectively.

Some examples of imaging through ball lenses and smaller microspheres obtained in this theses work are illustrated below. They show a qualitative agreement with the geometrical optics theory, but they also demonstrate some deviations from the geometrical optics theory which take place for smaller microspheres.

The results in Fig. 14 illustrate the resolution advantage of imaging through different microspheres over conventional microscope imaging performed without using microspheres. The experiments were performed using a Blu-ray disk object which is very convenient for this purpose since it has a period (~300 nm) which is just at the resolution limit of conventional imaging. The structure of the Blu-ray disk resolved by Atomic Force Microscope (AFM) is illustrated in Fig. 14(c). Better quality images can be obtained by scanning electron microscopy. It is not included in this thesis. The structure of a Blu-ray disk consists of 200 nm stripes separated by 100 nm gaps. This structure is hardly resolved by the best long working distance Mitutoyo 100× objective with NA=0.9, as shown in Fig. 14(a). However, this structure is resolved due to virtual imaging through polystyrene microspheres with n=1.59, as expected under contact conditions from Eq. (2). It can be clearly seen in the virtual images presented in Fig. 14(b). This structure is also resolved due to real imaging through BTG microspheres with a refractive index of around 1.9. These BTG microspheres with diameter D=25 μm are rather small which indicates that the results can deviate from the predictions of geometrical optics. The latter predicts that in the contact case, it should be still virtual imaging taking place in the experiments performed in the air. However, experiments indicate that the real image becomes observable under these conditions. This deviation of the experimental situation from the predictions of theory can be explained by some shortening of the focal distances compared to the prediction of geometrical optics for smaller microspheres. These

effects go beyond the scope of this thesis work because they require full-wave analysis and exact solution of Maxwell equations in the spirit of analysis performed in [16]. It should be also noted that most commonly BTG microspheres are used in a liquid environment. In the latter case, the refractive index contrast between the microspheres and surrounding media is significantly reduced and it becomes smaller than the corresponding critical value of parameter n_c indicating that the virtual imaging should take place. Indeed, under liquid immersion conditions we observed only virtual imaging similar to the observations of many groups working on applications of MAM technology.

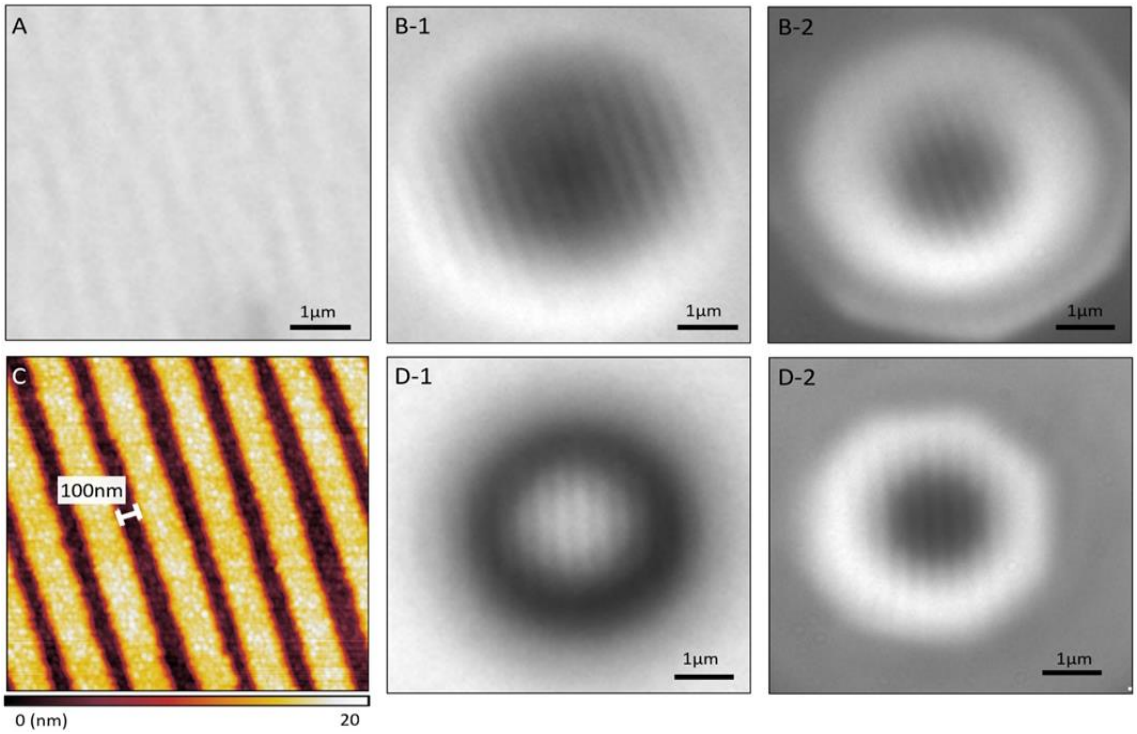

Figure 14: Blu-ray disc sample under various observation methods and conditions. (a) Illustrates an image captured with a 100× objective lens with a numerical aperture (NA=0.9.(b) Shows images captured with a 30-µm polystyrene (PS) microsphere, with sub-figures (B-1) and (B-2) displaying images taken with a 20x objective lens (NA =0.4) and a 50x objective lens (NA=0.9) respectively. (c) Presents results obtained using Atomic Force Microscopy (AFM). (d) Depicts an image captured with a 25-µm barium titanate glass (BTG) microsphere, with sub-figures (D-1) and (D-2) showcasing images captured using a 20x objective lens (NA=0.4) and a 50x objective lens (NA=0.9) respectively. The values indicated above each scale bar denote the length of the scale bar estimated in the real object scale [54].

After embedding the microspheres in the plastic coverslips, they were tested using a Mitutoyo microscope. Based on Eq. (2), BTG microspheres with an index of 2.1 are expected to produce real images in the case of an air environment. In the case of embedding such a high index microsphere in a plastic coverslip, the situation becomes much more complicated. On one hand, embedding should lead to a significant reduction of the refractive index contrast so that only virtual imaging is expected. On the other hand, this result is expected only in the case of complete embedding when the ball lens is enclosed with plastic around the entire surface. In practice, however, we found that the embedding was incomplete, in other words, the ball lenses were slightly extending from the coverslip. The amount of such extent varied from sample to sample, and it also depended on the ball lens diameter and temperature and pressure regimes. As a consequence of this partial extension of ball lenses from the coverslip, the results of imaging did not always follow the predictions of Eq. (2) obtained under the assumption of uniform embedding. The main goal of our fabrication was to increase FoV due to parallel observation through multiple ball lenses. Fig. 15(c) clearly shows that this concept works since we are able to see strongly magnified images through tenths of ball lenses at the same time. For larger ball lenses we also expect the same advantage, however, we were not able to fully use it because of the limitation of FoV imposed by our microscope camera. This is illustrated in Fig. 15(d) where the virtual image obtained through a single 550 μm ball lens takes the entire FoV offered by our microscope camera. Visual inspection through eyepieces shows that we have a similar advantage of parallel observation through multiple ball lenses in this case as well as similar to the case of smaller ball lenses. A CD was used instead of a Blu-ray disc in this experiment to show the capability of using an array of microspheres because CD has larger grooves.

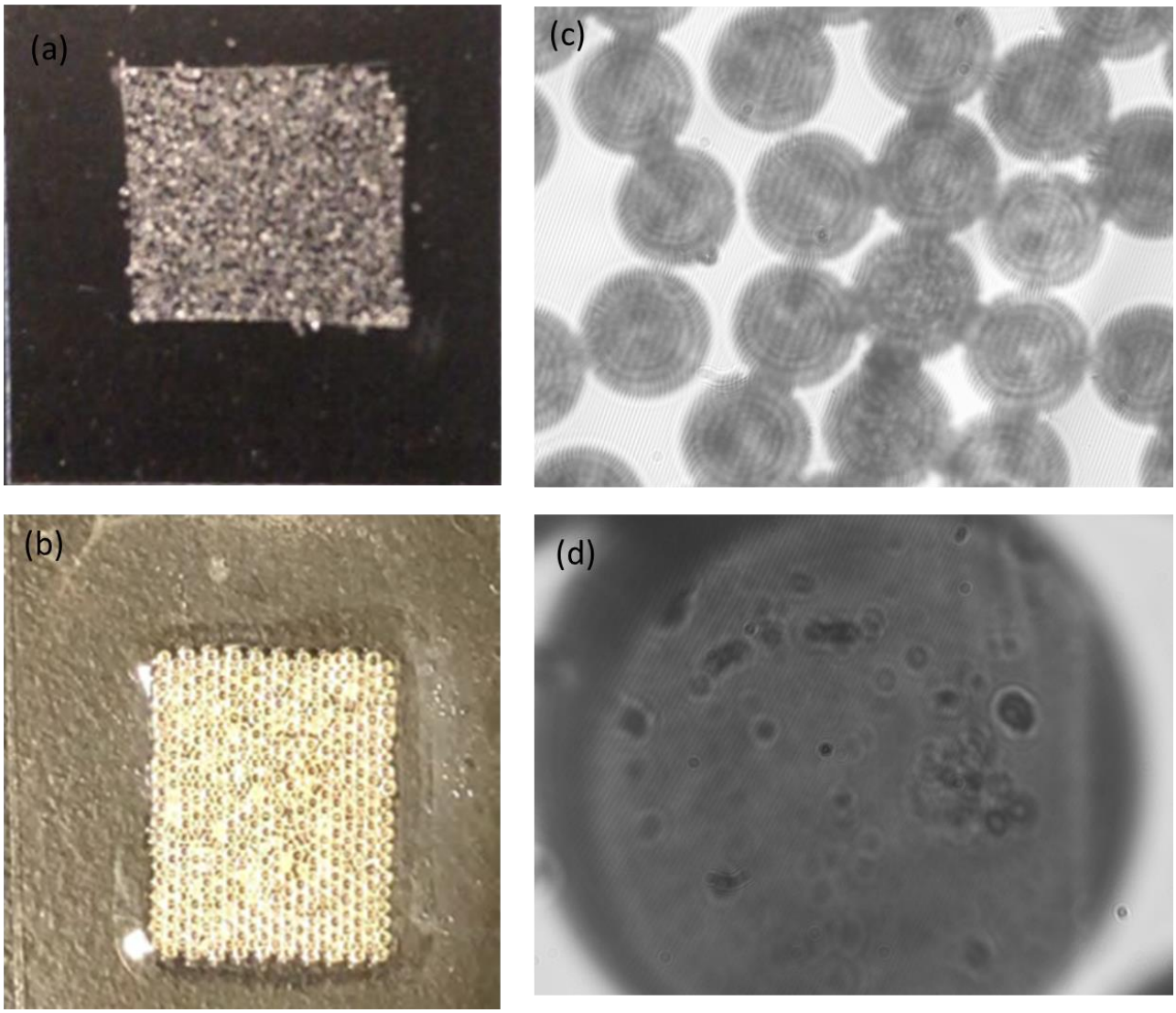

Figure 15: Imaging through coverslips with partly embedded BTG microspheres with the smaller (300 μm) and larger (550 μm) diameters illustrating the cases of real and virtual imaging, respectively. The amount of ball lens extension from the plastic coverslip in air is difficult to control for various ball lens diameters as well as for different temperature and pressure conditions leading in some cases to observation of both virtual and real images depending on the conditions. The case in (d) corresponds to virtual imaging, as expected from Eq. (2).

CHAPTER 3: BALL-LENS ASSISTED CELLPHONE MICROSCOPY

3.1. Experimental setup

To conduct this experiment, the Siemens star was positioned on the upright microscope stage to take advantage of the illuminator. An aperture, slightly exceeding 2 mm in size, was created on a piece of thin black cardboard. Within this aperture, the LASFN35 ball lens possessing a refractive index of n=2.02 was fixed inside the aperture in such a way that it was not moving inside it. The thin cardboard, housing the ball lens, was affixed to a manual X, Y stage micrometer with dimensions of 80X80 mm, enabling precise manipulation of the ball lens at a microscopic level. Simultaneously, the cellphone used in the experiment was affixed to a manual XYZ stage micrometer, introducing the capability to adjust the phone's position over the same distances as the ball lens. The phone was positioned approximately 3 mm away from the ball lens.

The experimental setup was designed to facilitate the high-resolution imaging of the Star Target obtained from Edmund optics though the ball lens using the cellphone.

The High-Resolution Microscopy Star Target shown in Figure 16, a well-established optical target, served as the object for evaluating the performance and characteristics of the optical system which is the ball lens-assisted cellphone imaging. The white light illuminator with the red spectral filter with about 10 nm bandwidth centered at λ=632 nm, integrated into the microscope, provided the maximal magnification for the LASFN ball lens with the refractive index n= 2.015 at this wavelength. The refractive indices of LASFN glass as a function of the wavelength can be

found following the link, https://www.swissjewel.com/materials/glass/lasfn-35/. According to Eq. (2) this means that very high magnifications are expected for these conditions because the imaging system operates at $n \approx n_c$.

Figure 16: High-Resolution Microscopy Star Target
https://www.edmundoptics.com/p/high-resolution-microscopy-star-target/38664/

The thin black cardboard, chosen as the material for the aperture, was meticulously selected for its properties, offering a suitable base for creating a precise opening closely matching the size of a 2 mm ball lens. This careful choice of material blocked the scattered light bypassing the ball lens and made possible domination of the image observed by the cell phone through the ball lens over scattered light coming from other areas of the sample.

The manual X, Y stage micrometer with an 80×80 (what is 80×80mm) configuration allowed micro manipulations of the ball lens. This stage allowed for controlled movements in both the *x* and *y* planes, enabling us to precisely position and manipulate the ball lens within the designated aperture. Thus, scanning of the ball lens over the sample was achieved not due to the shift of the ball lens, but due to the shift of the Siemens Star object. It was a more convenient setting for achieving precise step-by-step translation because we were able to use positional controls offered by the microscope translational stages.

Simultaneously, the cellphone was affixed to a manual XYZ stage micrometer. This stage, offering control in three dimensions, allowed us to finely adjust the position of the cellphone relative to the ball lens, as depicted in Figure 17. The ability to precisely match the movements of the phone with those of the ball lens was crucial for maintaining consistent experimental parameters. The placement of the cellphone approximately 3 mm away from the ball lens was a decision aimed at optimizing the experimental setup. This allowed us to realize a close up imaging similar to that used in infinity-corrected microscope objectives.

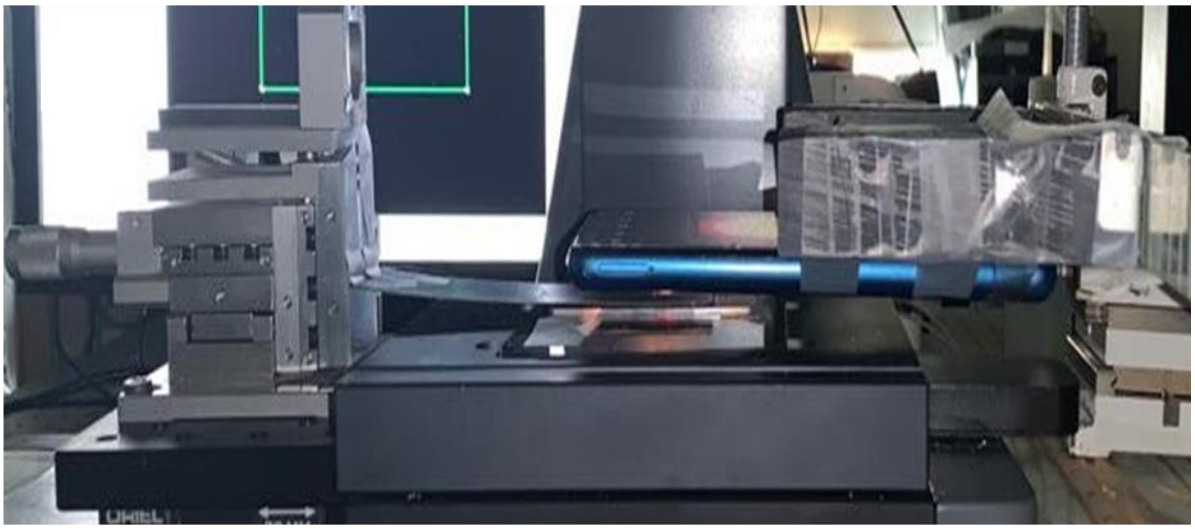

Figure 17: Experimental setup. This image shows the arrangement of the setup.

3.2. Ball-lens translation and image stitching

An XY-axis manual linear translation stage was used to translate the ball lens over the Siemens star surface. It was not used for precise step-by-step scanning of the sample, but it created an additional flexibility for our setup allowing us to change the position of the ball lens. Scanning the surface of the sample by the ball lens allows the increased FoV which is necessary for practical use of this imaging system in biomedical applications where large areas of the samples need to be inspected. As the experiment unfolded, the movements of the micrometer stages allowed for systematic variations of the position of the ball lens and cellphone, as depicted in Figure 18. This systematic movement was aimed at taking different images at different positions to later stitch together. Different configurations and alignments influenced the optical outcomes observed through the cellphone. Throughout the experiment, the images collected were carefully documented, noting any changes in the appearance of the Siemens star as observed through the cellphone.

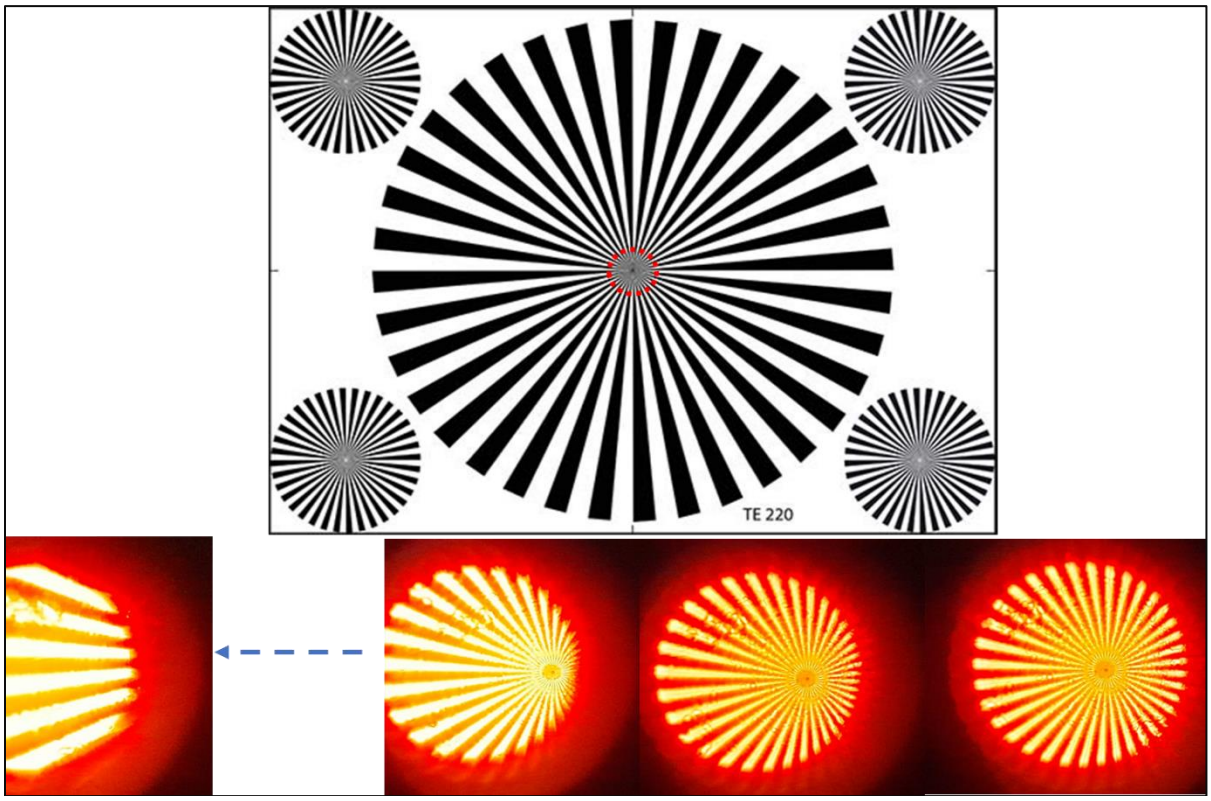

Figure 18: Image of the star target. Highly resolved images were taken at different locations with the translations of the ball lens from right to left.

Image stitching also referred to as photo stitching, was used this method to merge several photographic images that have overlapping features. This process aims to create a segmented panorama or a high-resolution image. The stitched images were precisely overlapped to achieve a seamless outcome as shown in Figure 19(b) (it looks Fig. 19(a) is missing, it is strange that this figure begins from (b) part without showing (a) part, please correct).

The findings were achieved utilizing a cellphone utilizing a close-up imaging similar to infinity objectives achieved in our case using the millimeter scale contact ball lenses with index of refraction approaching n_c=2 value. The resulting image quality is similar to that of standard microscopy employing a 10× objective with a restricted FoV of 0.1D. This same strategy can be implemented to achieve high-quality images of biological specimens. For instance, consider the case in which the resolution is high enough to scrutinize the spatial layout of tumor-infiltrating lymphocytes (TILs) in the stained histological melanoma specimens. The maximal magnification ($M > 50$) with the highest resolution (≈0.66 μm at λ = 589 nm) was obtained for contact imaging of nanoplasmonic structures [55,56]. By taking advantage of the dispersive properties, $n(\lambda)$, of the material from which the LASFN35 ball lenses are made, it was discovered that chromatic aberration occurs near the critical index of two.

In general, more detailed studies performed with nanoplasmonic structures in Ref. [55,56] demonstrate a possibility to increase the resolution up to a level where it is not limited any more by pixelation of the camera sensor array. Under conditions of maximal image magnification, a transition to diffraction-limited resolution has been demonstrated in [55,56]. By examining the characteristics of a glass ball lens, this study suggests that incorporating glass ball lenses into cell

phone camera attachments could lead to the making of an inexpensive cell phone microscope accessible to the public. If glass ball lenses have an index of refraction of around 2, they could provide significantly higher magnifications. Indeed, they can exceed the quality of imaging offered the 10× objective lens of a common microscope. Moreover, close-up imagery using a macro lens, like one in previous research [47], suggests that a single ball lens can provide an expanded field of view of over 200µm, with further possibilities of enlargement by moving the lenses themselves.

In Figure 19, the images of the Star Target, captured by the Samsung Galaxy M12 (Model: SM-M127G/DS) phone with LASFN35 lens of 2mm diameter at 632 nm. Figure 16(b) shows the images obtained at different positions of the ball lens which were cropped and combined without using any stitching software tools.

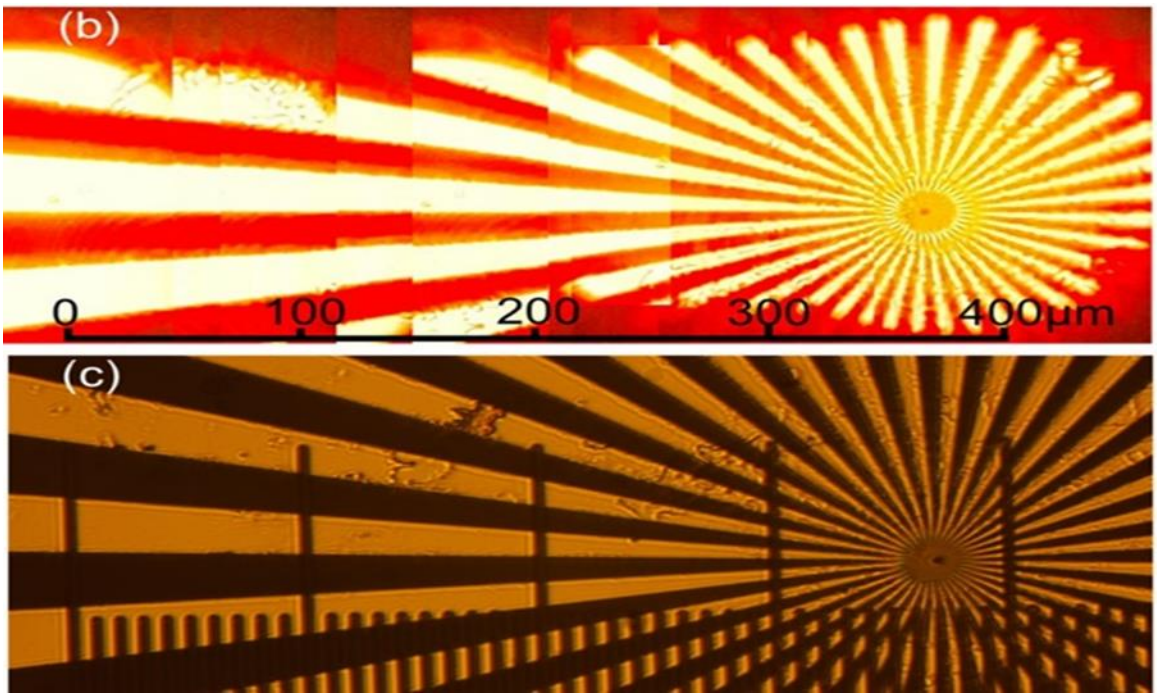

Figure 19: Demonstrates the expansion of the field-of-view (FoV) through the translation of a 2 mm LSFN35 ball lens, coupled with close-up imaging at a distance (d = 10 mm) and a wavelength (λ) of 632 nm. (b) A combination of cropped images captured at various positions of the ball lens illustrates a total FoV of 0.5 mm with an approximate resolution of 1.5 µm. (c) The

widefield microscopy image of the Siemens star, alongside the calibration ruler (with smaller divisions measuring 10 μm), was captured using the Mitutoyo 10× objective (NA = 0.25) [55].

In evaluating the resolution of the image obtained through the ball lens imaging system assisted by a cellphone, we adopted a simplified approach. A ruler featuring 0.01 mm divisions was chosen as the calibrating object for finding real physical dimensions in the object plane. The resulting cellphone image obtained through the ball lens was subjected to detailed analysis utilizing ImageJ software to facilitate the conversion of the 0.01 mm divisions into pixels as shown in Figure 20. The conversion process revealed that each 0.01 mm division on the ruler corresponded to a representation of 18 pixels in the captured image. This transformation provided a calibration factor, essentially bridging the physical scale of the ruler with the digital representation in pixels. Such calibration was important for ensuring accuracy in subsequent assessments of the system's resolution. This calibration was used to quantify the resolution of the Siemens star. Establishing the pixel-to-millimeter relationship allowed us to perform a comprehensive analysis of the Siemens star image's resolution.

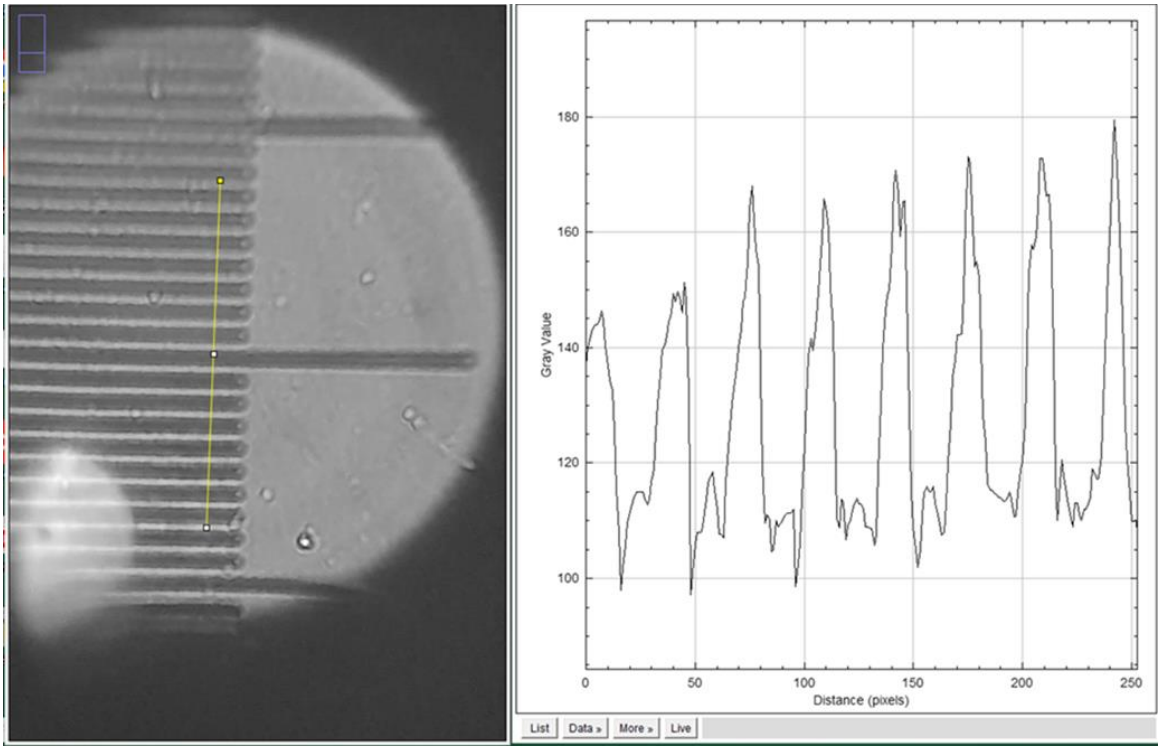

Figure 20: Cellphone imaging of the 0.01mm ruler division using the LASFN35 ball lens with n = 2.015 and D = 2.0 mm.

From the cellphone-assisted ball lens image, two specific trips were chosen for analysis to help quantify the resolution. At three distinct locations, represented by Figures 21(a), 21(b), and 21(c), the intensity profiles were measured. These measurements resulted in the generation of three distinct curves, each illustrating the intensity profile at different radial distances illustrating the resolution of different spatial periods within the Siemens star target. Figures 21(d), 21(e), and 21(f) are the intensity profiles of figures 21(a),21(b), and 21(c). As the bar was moved toward the center, the radius of the intensity profile got smaller as depicted in Figures 21(a), 21(b), and 21(c). The radiuses were estimated to be 107µm, 64µm, and 31µm.

The usual procedure of resolution quantification involves calculations of the images by convoluting objects with PSF. The fitting parameter is the width of PSF which is varied in such calculation to achieve the closest fit to the experimentally measured intensity profiles through very small objects with arbitrary shapes. Once such a fit is optimized, the width of the corresponding PSF can be associated with the resolution of the system based on the Houston

resolution criterion. This procedure was used for the resolution quantification in the case of using bow ties or other nanoplasmonic objects, and it worked well in previous studies.

In this work, we selected a somewhat easier and simpler route to quantify the resolution without using a more rigorous procedure of convolution with PSF. Our process does not possess the same rigor and accuracy as the more mathematically based procedure described above, but it has the advantage of being a very obvious way of semi-quantitative determination of resolution based on visual inspection of images applicable specifically to the case of Siemens star object.

The idea is that far away from the center, the transversal period is much larger than the resolution of the system and we have very large intensity modulation from spoke to spoke indicating that the structure is fully resolved. If we move close to the center, the transversal period is reduced, and one can expect a reduction of the intensity modulation depth in the corresponding intensity profiles. If we continue moving closer to the center, at some radial distance the modulation depth becomes comparable to the random fluctuations in the intensity profiles which means that we are losing the ability to discern the individual spokes. As a result, at radial distances shorter than this critical distance we cannot resolve the structure and at radial distances larger than this critical distance we can resolve the structure. This means this particular radial distance approximately corresponds to the resolution limit of our system. As a semi-quantitative measure of the resolution, we can take the period of the spokes at the radial distance corresponding to this critical distance. All we need to do to realize this procedure is to measure the critical radial distance in microns and then take into account that in our Siemens star target we have 36 pairs (black and white regions) of spokes.

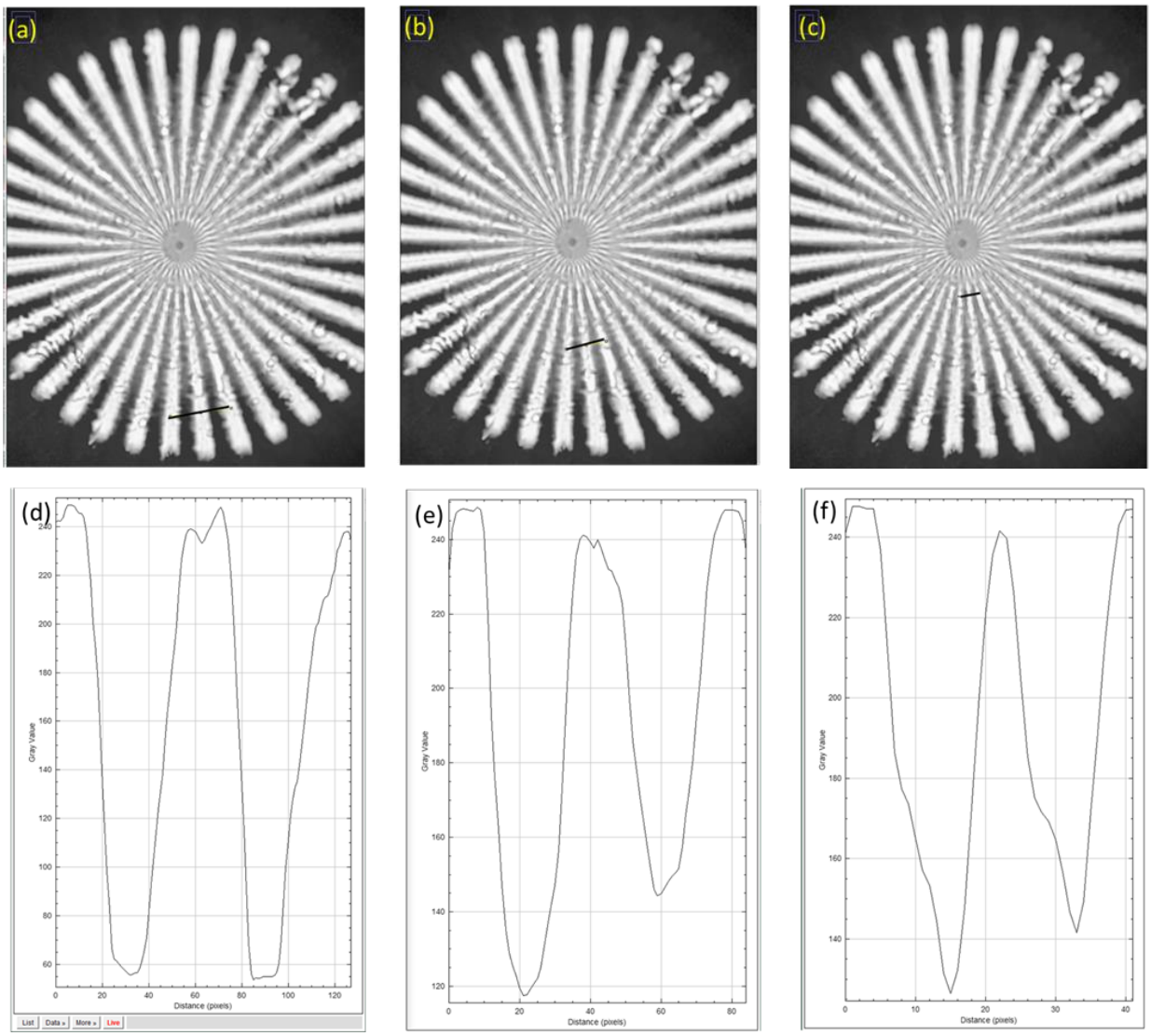

Figure 21: The intensity profile at different radial distance illustrating resolution for different spatial periods of the Siemens star target.

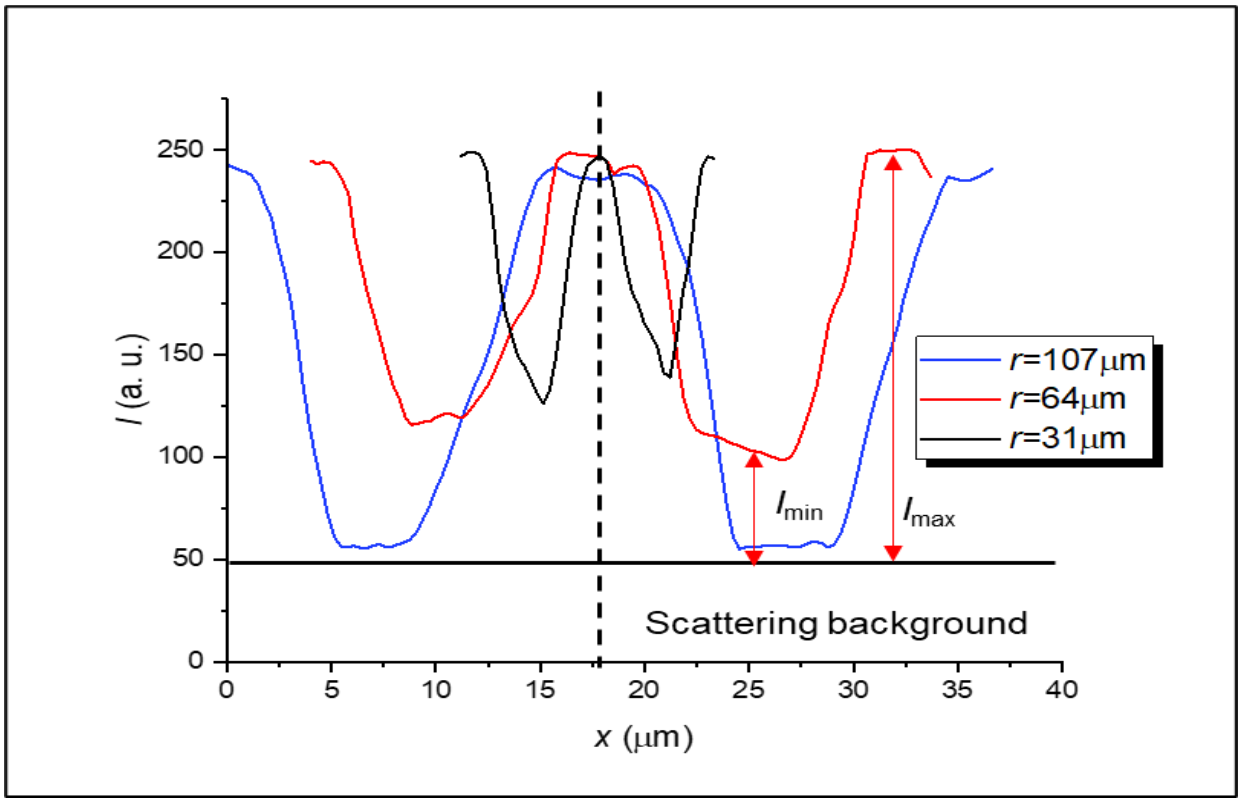

Figure 22: Comparative representation of the intensity profiles taken at different radial distances for the Siemens star target. Estimated radial distances 107, 64, and 31 μm are shown in the legend to indicate the colors of the corresponding curves.

The reduction of the modulation depth in the intensity profiles as we move towards the center of the Siemens star target is better seen in Fig. 22 which illustrates profiles taken at the radial distances 107, 64, and 31 μm. One more feature of the transmission microscopy used in our experiment is the existence of a certain illumination level due to the presence of scattered light. To enhance the visibility of the object we used a diffuser placed several millimeters below the sample. This scattered light was present everywhere along the image. It could be easily checked by inspecting larger areas that were not transparent – scattered light was present in these areas. Determination of the exact level of scattered light was a separate and complicated task and we did not pursue this goal in this work. However, to simply illustrate the approximate level of scattered light, we indicated where we expect it to be by the horizontal line in Figure 22. Had we performed

a rigorous resolution quantification based on convolution with PSF, this scattering background level would have been taken into account in our resolution quantification. We should conclude that in any case all three profiles in Fig. 21 are fully resolved.

In our simplified method, however, we simply continue moving towards the center of the Siemens star object, as illustrated by the intensity profiles in Fig. 23. The modulation depth of the intensity profiles further drops which means that we approach the "circle of indistinguishability" near the center of Siemens star target. With one small remaining step, we can determine the critical distance from the center where the resolution criterion is approximately satisfied. This was done by moving further toward the center which allowed us to determine that this critical distance is approximately equal to $2\pi r/36$ where r is the critical distance in μm that, in turn, allows estimating the resolution at approximately 1.5 μm level in our experiments. This is a somewhat lower resolution than that determined in previous studies [55,56] using illumination with spectrally filtered light. It should be noted that closer to the "circle of indistinguishability" the intensity profile experiences a phase shift by π, as illustrated in Fig. 24. We experimentally tested that this effect depends on the position of the focusing plane. Generally, the study of this effect goes beyond the scope of this thesis. We believe that it is related to the interference properties taking place in regions of Siemens star target with very short periods comparable to the resolution of the system. In future work, experiments can be performed with narrow spectral filters and the resolution quantification can be performed using a more rigorous procedure based on convolution with PSF. They will provide more precise resolution values and, potentially, shed more light on the nature of the π shift effect illustrated in Fig. 24.

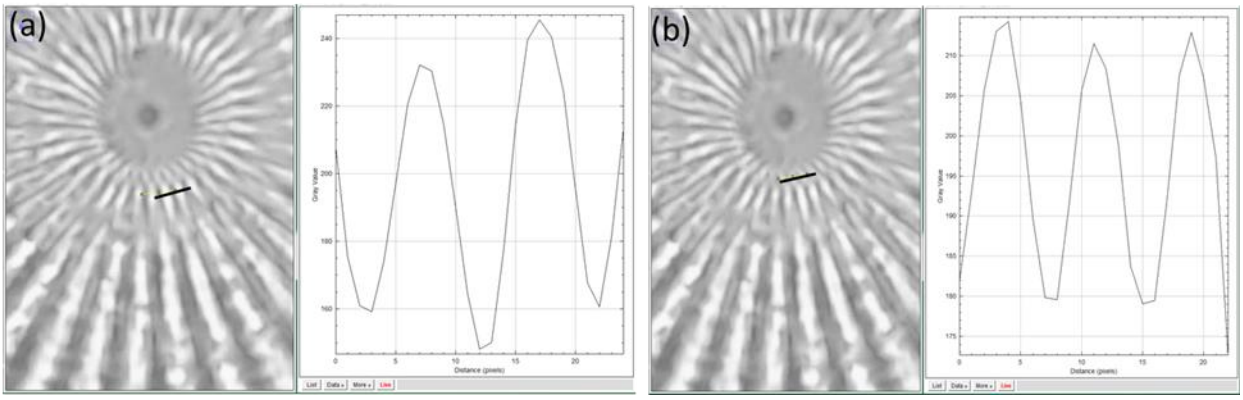

Figure 23: Image near the center of indistinguishability. (a) First shifted image (b) Second shifted image.

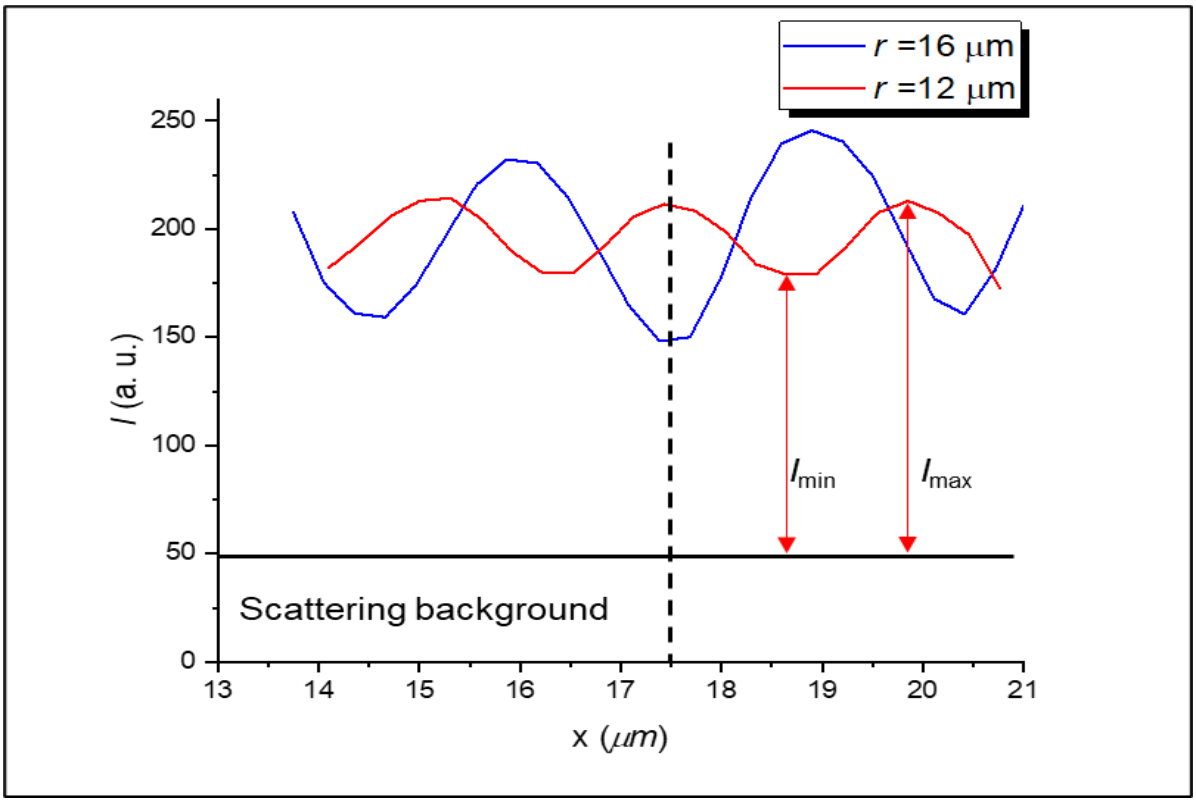

Figure 24: Intensity distribution Illustrating an effect of π phase shift. The image intensity distribution Illustrates an effect of π phase shift experienced by the profiles. This effect

depends on the position of the focusing plane. Its nature is probably related to interference properties taking place at very short periods, but we did not study this effect in this thesis work assuming that it will be studied in future work.

REFERENCES

1. Abbe, E. Beiträge zur Theorie des Mikroskops und der mikroskopischen Wahrnehmun, Archiv. Für Mikroskopische. Anatomie. 1873, 9, 413.

2. S. W. Hell, S. J. Sahl, M. Bates, X. Zhuang, R. Heintzmann, M. J. Booth, J. Bewersdorf, G. Shtengel, H. Hess, P. Tinnefeld, A. Honigmann, S. Jakobs, I. Testa, L. Cognet, B. Lounis, H. Ewers, S. J. Davis, C. Eggeling, D. Klenerman, K. I. Willig, G. Vicidomini, M. Castello, A. Diaspro, T. Cordes, The 2015 super-resolution microscopy roadmap, J. Phys. D: Appl. Phys. 2015, 48, 443001.

3. B. R. Masters, Superresolution Optical Microscopy, 1st ed. Springer, Cham, 2020, ISBN 978-3-030-21690-0.

4. V. Astratov, Label-Free Super-Resolution Microscopy, Springer Nature, Switzerland 2019.

5. Astratov, V.N.; Sahel, Y.B.; Eldar, Y.C.; Huang, L.; Ozcan, A.; Zheludev, N.; Zhao, J.; Burns, Z.; Liu, Z.; Narimanov, E.; et al., Roadmap on Label-Free Super-Resolution Imaging, Laser Photonics Rev. 2023, 17, 2200029.

6. C. J. R. Sheppard, Resolution and super-resolution, Microsc. Res. Tech. 80, 590–598 (2017).

7. Z. Wang, W. Guo, L. Li, B. Luk'yanchuk, A. Khan, Z. Liu, Z. Chen, and M. Hong, "Optical virtual imaging at 50 nm lateral resolution with a white-light nanoscope," Nat. Commun. 2, 218 (2011).

8. L. A. Krivitsky, J. J. Wang, Z. Wang, and B. Luk'yanchuk, "Locomotion of microspheres for super-resolution imaging," Sci. Rep. 3, 3501 (2013).

9. V.N. Astratov and A. Darafsheh, Methods and Systems for Super-Resolution Optical Imaging Using High-Index of Refraction Microspheres and Microcylinders, US patent 9726874, on 08/17/2014.

10. A. Darafsheh, G.F. Walsh, L. Dal Negro, and V.N. Astratov, Optical Super-Resolution by High-Index Liquid-Immersed Microspheres, Appl. Phys. Lett. 101, 141128 (2012).

11. L. Li, W. Guo, Y. Yan, S. Lee, and T. Wang, "Label-free super-resolution imaging of adenoviruses by submerged microsphere optical nanoscopy," Light 2, e104 (2013).

12. F. Wang, L. Liu, H. Yu, Y. Wen, P. Yu, Z. Liu, Y. Wang, and W. J. Li, Scanning superlens microscopy for non-invasive large field-of-view visible light nanoscale imaging," Nat. Commun. 7, 13748 (2016).

13. A. Darafsheh, N. I. Limberopoulos, J. S. Derov, D. E. Walker, Jr., and V. N Astratov, "Advantages of microsphere-assisted super-resolution imaging technique over solid immersion lens and confocal microscopies," Appl. Phys. Lett 104, 061117 (2014).

14. Aguilar, Alberto, et al. "Label-Free Super-Resolution Imaging below 90-Nm Using Photon-Reassignment." Open Research Europe, vol. 1, 2021, pp. 3, https://doi.org/10.12688/openreseurope.13066.1.

15. S. M. Mansfield and G. S. Kino, Solid immersion microscope, Appl. Phys. Lett. 57, 2615–2616 (1990).

16. A. V. Maslov, B. Jin, and V. N. Astratov, "Wave optics of imaging with contact ball lenses," Sci. Rep. 13, 6688 (2023).

17. Y. Duan, G. Barbastathis, and B. Zhang, "Classical imaging theory of a microlens with super-resolution," Opt. Lett. 38, 2988–2990 (2013).

18. V. M. Sundaram and S.-B. Wen, "Analysis of deep sub-micron resolution in microsphere based imaging," Appl. Phys. Lett. 105, 204102 (2014).

19. T. X. Hoang, Y. Duan, X. Chen, and G. Barbastathis, "Focusing and imaging in microsphere-based microscopy," Opt. Express 23, 12337–12353 (2015).

20. A. V. Maslov and V. N. Astratov, "Imaging of sub-wavelength structures radiating coherently near microspheres," Appl. Phys. Lett. 108, 051104 (2016).

21. A. V. Maslov and V. N. Astratov, Optical Nanoscopy with Contact Mie-Particles: Resolution Analysis, Appl. Phys. Lett. 110, 261107 (2017).

22. A. V. Maslov and V. N. Astratov, "Resolution and reciprocity in microspherica nanoscopy: Point-spread function versus photonic nanojets," Phys. Rev. Appl. 11, 064004 (2019).

23. A. V. Maslov and V. N. Astratov, "Origin of the super-resolution of microsphere-assisted imaging," Appl. Phys. Lett. 124, 061105 (2024).

24. A. V. Kanaev, V. N. Astratov, and W. Cai, "Optical coupling at a distance between detuned spherical cavities," Appl. Phys. Lett. 88, 111111 (2006).

25. K.W. Allen, N. Farahi, Y. Li, N.I. Limberopoulos, D.E. Walker Jr., and V.N. Astratov, “Super-Resolution Imaging by Arrays of High-Index Spheres Embedded in Transparent Matrices,” IEEE Proc. of National Aerospace and Electonics Conference, Dayton, Ohio, June 25-27, 2014, p.52-54.

26. K. W. Allen, N. Farahi, Y. Li, N. I. Limberopoulos, D. E. Walker, A. M. Urbas, et al., "Super-resolution microscopy by movable thin-films with embedded microspheres: Resolution analysis", Ann. Phys. (Berlin), vol. 527, pp. 513-522, 2015.

27. K. W. Allen, Y. Li and V. N. Astratov, "Comment on ‘Super-resolution microscopy by movable thin-films with embedded microspheres: Resolution analysis’ [Ann. Phys. (Berlin) 527 513 (2015)]", Ann. Phys, vol. 528, pp. 901-904, 2016.

28. K. W. Allen Waveguide, Photodetector, and Imaging Applications of Microspherical Photonics (PhD thesis, Univ. North Carolina at Charlotte, 2014).

29. A. Brettin, F. Abolmaali, K. F. Blanchette, C. L. McGinnis, Y. E. Nesmelov, N. I. Limberopoulos, D. E. Walker, Jr., I. Anisimov, A. M. Urbas, L. Poffo, A. V. Maslov, and V. N. Astratov, “Enhancement of resolution in microspherical nanoscopy by coupling of fluorescent objects to plasmonic metasurfaces,” Appl. Phys. Lett. 114, 131101 (2019).

30. V.N. Astratov, N.I. Limberopoulos, and A. Urbas, Super-Resolution Microscopy Methods and Systems Enhanced by Dielectric Microspheres and Metallic Nanostructures, US patent 9835870, on 12/05/1917.

31. V. N. Astratov, Arrays of Superlenses for Super-Resolution Optical Imaging with Wide Field-of-View, US nonprovisional patent application 17/143,445 filed on 01/07/2021. Publication US20210208414A1 on 07/08/2021. US Patent 11,762,214, on 9/19/2023.

32. D. M. Whittaker, I. S. Culshaw, V. N. Astratov, and M. S. Skolnick, Photonic Bandstructure of Patterned Waveguides with Dielectric and Metallic Cladding, Phys.Rev.B 65, 073102 (2002).

33. A.D. Bristow, V.N. Astratov, R. Shimada, I.S. Culshaw, M.S. Skolnick, D.M. Whittaker, A. Tahraoui, and T.F. Krauss, Polarization Conversion in the Reflectivity Properties of Photonic Crystal Waveguides, IEEE J.of Q.El. 38, 880-884 (2002).

34. A.D. Bristow, D.M. Whittaker, V.N. Astratov, M.S. Skolnick, A. Tahraoui, T.F. Krauss, M. Hopkinson, M.P. Croucher, and G.A. Gehring, Defect States and Commensurability in Dual-Period AlxGa1-xAs Photonic Crystal Waveguides, Phys.Rev.B 68, 033303 (2003).

35. D. Lange, C. W. Storment, C. A. Conley, G. T. A. Kovacs, A microfluidic shadow imaging system for the study of the nematode Caenorhabditis elegans in space, Sens. Actuators, B 2005, 107, 904.

36. X. Heng, D. Erickson, L. R. Baugh, Z. Yaqoob, P. W. Sternberg, D. Psaltis, C. Yang, Optofluidic microscopy—a method for implementing a high-resolution optical microscope on a chip, Lab Chip 2006, 6, 1274.

37. J. Garcia-Sucerquia, W. Xu, S. K. Jericho, P. Klages, M. H. Jericho, H. J. Kreuzer, Digital in-line holographic microscopy, Appl. Opt. 2006, 45, 836.

38. D. Tseng, O. Mudanyali, C. Oztoprak, S. O. Isikman, I. Sencan, O. Yaglidere, A. Ozcan, Lensfree microscopy on a cellphone, Lab Chip 2010, 10, 1787.

39. Z. J. Smith, K. Chu, A. R. Espenson, M. Rahimzadeh, A. Gryshuk, M. Molinaro, D.M. Dwyre, S. Lane, D. Matthews, S.Wachsmann-Hogiu, Cell-Phone-Based Platform for Biomedical Device Development and Education Applications, PLoS One 6, e17150 (2011).

40. I. Bogoch, J. Andrews, B. Speich, J. Utzinger, S. Ame, S. M. Ali, J. Keiser, Mobile phone microscopy for the diagnosis of soil-transmitted helminth infections: a proof-of-concept study, Am. J. Trop. Med. Hyg. 88,626-629 (2013).

41. Y. Kobori, P. Pfanner, G. S. Prins, C. Niederberger, Novel device for male infertility screening with single-ball lens microscope and smartphone, Fertil. Steril. 106, 574—578 (2016)

42. T. E. Agbana, J.-C. Diehl, F. van Pul, S. M. Patlan, M. Verhaegen, G. Vdovin, Imaging & identification of malaria parasites using cellphone microscope with a ball lens, PLoS One 13, e0205020 (2018).

43. F. Abolmaali, A. Brettin, A. Green, N.I. Limberopoulos, A.M. Urbas, and V.N. Astratov, Photonic Jets for Highly Efficient Mid-IR Focal Plane Arrays with Large Angle-of-View, Opt. Express 25, 31174-31175 (2017).

44. F. Abolmaali, A. Brettin, N.I. Limberopoulos, A.M. Urbas, and V.N. Astratov, Use of Photonic Jets Produced by Dielectric Microspheres for Increasing Sensitivity and Angle-of-View of MWIR Detectors, Proc. of SPIE 2017, 7 pp. Phot. West, San Francisco, Jan. 28-Feb 2 (2017).

45. K.W. Allen, F. Abolmaali, J.M. Duran, G. Ariyawansa, N.I. Limberopoulos, A.M. Urbas, and V.N. Astratov, Increasing Sensitivity and Angle-of-View of Mid-Wave Infrared Detectors by Integration with Dielectric Microspheres, Appl. Phys. Lett. 108, 241108 (2016).

46. A. Brettin, F. Abolmaali, N.I. Limberopoulos, A. Green, I. Anisimov, A. M. Urbas, and V.N. Astratov, Towards Fabrication of Mid-IR FPAs with Enhanced Sensitivity and Reduced Dark Current by Using Integration with Microspherical Arrays, IEEE Proc. of National Aerospace and Electonics Conference, Dayton, Ohio, July 23-26, 3 pp., 2018.

47. V.N. Astratov, K.W. Allen, N.I. Limberopoulos, A. Urbas, and J. M. Duran, Photodetector focal plane array systems and methods, US patent 9362324, on 06/07/2016.

48. V.N. Astratov, A. Brettin, N.I. Limberopoulos, and A. Urbas, Photodetector Focal Plane Array Systems and Methods Based on Microcomponents with Arbitrary Shapes, US patent 10585238, on 03/10/2020.

49. V.N. Astratov, A. Brettin, F. Abolmaali, C.L. McGinnis, K.F. Blanchette, Y.E. Nesmelov, A.V. Maslov, N.I. Limberopoulos, D.E. Walker Jr., and A.M. Urbas, Spotlight on Microspherical Nanoscopy: Experimental Quantification of Super-Resolution, IEEE Proc. of Int. Conf. on Transparent Opt. Networks – ICTON'17, 1st Workshop on Label-Free Super-Resolution and Sensing, Girona, Spain, July 2-6, 2017, 4pp., We.D6.1.

50. A. Brettin,C.L. McGinnis, K.F. Blanchette, Y.E. Nesmelov, N.I. Limberopoulos, D.E. Walker Jr., A.M. Urbas, and V.N. Astratov, Quantification of Resolution in Microspherical Nanoscopy with Biological Objects, IEEE Proc. of National Aerospace and Electonics Conference, Dayton, Ohio, June 27-30, 4 pp., 2017.

51. V.N. Astratov, A. Brettin, F. Abolmaali, L. Poffo, and A.V. Maslov, Plasmonics and Superresolution in Microspherical Nanoscopy, IEEE Proc. of Int. Conf. on Transparent Opt. Networks – ICTON'18, 2nd Workshop on Label-Free Superresolution and Sensing, Bucharest, Romania, July 1-5, 2018, 4pp., We.B6.3.

52. A. Brettin, C.L. McGinnis, F. Abolmaali, N.I. Limberopoulos, D. Walker, A.M. Urbas, L. Poffo, A.V. Maslov, and V.N. Astratov, Superresolution Imaging of Fluorescent Nanospheres by Using High-Index Microspheres Embedded in Slabs with Illumination Provided by Plasmonic Array, IEEE Proc. of National Aerospace and Electonics Conference, Dayton, Ohio, July 23-26, 3 pp., 2018.

53. V.N. Astratov, F. Abolmaali, A. Brettin, G.W. Bidney, B. Jin, N.I. Limberopoulos, D.E. Walker, H. Li, and A.V. Maslov, Resolution Enhancement in Microspherical Nanoscopy by Coupling of Emission to Plasmonics Metasurfaces, IEEE Proc. of Int. Conf. on Transparent Opt. Networks – ICTON'19, 3rd Workshop on Label-Free Superresolution and Sensing, Angers, France, July 9-16, 4pp., 2019.

54. H. S. S. Lai, F. Wang, Y. Li, B. Jia, L. Liu, W. J. Li, Super-resolution real imaging in microsphere-assisted microscopy. PLoS ONE 2016, 11, e0165194.

55. B. Jin, A. R. Jean, A. V. Maslov, V. N. Astratov, Ball Lens-Assisted Cellphone Imaging with Submicron Resolution, Laser Photon. Rev., 2300146 (2023).

56. B. Jin, Superlens Imaging and Light Concentration in Mesoscale Photonics: Design and Implementation, (PhD thesis, Univ. North Carolina at Charlotte, 2022).

57. G.W. Bidney, A. Brettin, B. Jin, N.I. Limberopoulos, I. Anisimov, H. Li, A.V. Maslov, and V.N. Astratov, Improving Cellphone Microscopy Imaging with Contact Ball Lenses, IEEE Proc. of National Aerospace and Electonics Conference, Dayton, Ohio, July 15-19, 4 pp., to be published 2019.

58. B. Jin, G.W. Bidney, I. Anisimov, N.I. Limberopoulos, A.V. Maslov, and V. N. Astratov, High-resolution label-free cellphone microscopy using contact ball lenses, IEEE Proc. of National Aerospace and Electonics Conference, Dayton, Ohio, August 16-19, 2021, pp. 356-358 (2021).

59. B. Jin, G.W. Bidney, I. Anisimov, N.I. Limberopoulos, K.W Allen, A.V. Maslov, V.N. Astratov, "Label-free cellphone microscopy with submicron resolution through high-index contact ball lens for in vivo melanoma diagnostics and other applications," Proc. SPIE 11972, Label-free Biomedical Imaging and Sensing (LBIS) 2022, 119720F (2 March 2022).

60. V.N. Astratov, B.Jin, A.A. Erykalin, and A.V. Maslov, "Ball lens-assisted smartphone microscopy with diffraction-limited resolution," Proc. SPIE 12152, Mesophotonics: Physics and Systems at Mesoscale, 1215206 (24 May 2022).

61. K. W. Allen, N. Farahi, Y. Li, N. I. Limberopoulos, D. E. Walker Jr., A. M. Urbas, and V.N. Astratov, Overcoming the Diffraction Limit of Imaging Nanoplasmonic Arrays by Microspheres and Microfibers, Opt. Express 23, 24484-24496 (2015).

62. K. W. Allen, V. Liberman, M. Rothschild, N. I. Limberopoulos, D. E. Walker Jr., A. M. Urbas, and V. N. Astratov, Deep-UV Microsphere-Assisted Ultramicroscopy, IEEE Proc. of Int. Conf. on Transparent Opt. Networks – ICTON'15, Special Section on Photonic Atoms and Molecules, Budapest, Hungary, July 5-9, 2015, 4pp., paper We.P.26.

63. K. W. Allen, N. Farahi, Y. Li, N. I. Limberopoulos, D. E. Walker Jr., A. M. Urbas, V. Liberman, and V. N. Astratov, "Super-Resolution by Microspheres and Fibers – Myth or Reality?", IEEE Proc. of Int. Conf. on Transparent Opt. Networks – ICTON'15, Special Section on Photonic Atoms and Molecules, Budapest, Hungary, July 5-9, 2015, 4pp., paper We.C6.1.

64. V. N. Astratov, A. V. Maslov, K. W. Allen, N. Farahi, Y. Li, A. Brettin, N. I. Limberopoulos, D. E. Walker Jr., A. M. Urbas, V. Liberman, and M. Rothschild, Fundamental limits of super-resolution

microscopy by dielectric microspheres and microfibers, Proc. of SPIE, Vol. 9721, 97210K, 7 pp. (2016).

65. A. Brettin, F. Abolmaali, N.I. Limberopoulos, D.E. Walker Jr., A.M. Urbas, and V.N. Astratov, Superresolution Imaging with Contact Microspheres: Importance of Numerical Aperture, IEEE Proc. of Int. Conf. on Transparent Opt. Networks – ICTON'16, Special Section on Photonic Atoms and Molecules, Trento, Italy, July 10-14, 2016, 4pp.

66. V.N. Astratov, F. Abolmaali, A. Brettin, K.W. Allen, A.V. Maslov, N.I. Limberopoulos, D. E. Walker Jr., and A.M. Urbas, Label-Free Nanoscopy with Contact Microlenses: Super-Resolution Mechanisms and Limitations, IEEE Proc. of Int. Conf. on Transparent Opt. Networks – ICTON'16, Special Section on Photonic Atoms and Molecules, Trento, Italy, July 10-14, 2016, 4pp.

67. A. Brettin, F. Abolmaali, N.I. Limberopoulos, D.E. Walker Jr., A.M. Urbas, and V.N. Astratov, Imaging of Two-Dimensional Nanoplasmonic Structures by Nanoscopy with Contact Microlenses and Various Microscope Objectives, IEEE Proc. of National Aerospace and Electonics Conference, Dayton, Ohio, July 25-29, 4 pp., 2016.

68. A. Brettin, K.F. Blanchette, Y. Nesmelov, N.I. Limberopoulos, A.M. Urbas, and V.N. Astratov, Microsphere Nanoscopy for Imaging of Actin Proteins, IEEE Proc. of National Aerospace and Electonics Conference, Dayton, Ohio, July 25-29, 3 pp., 2016.

69. V. N. Astratov, A. V. Maslov, A. Brettin, K. F. Blanchette, Y. E. Nesmelov, N. I. Limberopoulos, D. E. Walker Jr., and A. M. Urbas, Contact Microspherical Nanoscopy: From Fundamentals to Biomedical Applications, Proc. of SPIE 2017, 7pp. Phot. West, San Francisco, Jan. 28-Feb. 2 (2017) Nanoscale Imaging, Sensing, and Actuation for Biomedical Applications XIV, edited by Alexander N. Cartwright, Dan V. Nicolau, Proc. of SPIE Vol. 10077, 100770S

70. V.N. Astratov, A. Brettin, F. Abolmaali, C.L. McGinnis, K.F. Blanchette, Y.E. Nesmelov, A.V. Maslov, N.I. Limberopoulos, D.E. Walker Jr., and A.M. Urbas, Spotlight on Microspherical Nanoscopy: Experimental Quantification of Super-Resolution, IEEE Proc. of Int. Conf. on Transparent Opt. Networks – ICTON'17, Girona, Spain, July 2-6, 2017, 4pp.

71. A. Brettin,C.L. McGinnis, K.F. Blanchette, Y.E. Nesmelov, N.I. Limberopoulos, D.E. Walker Jr., A.M. Urbas, and V.N. Astratov, Quantification of Resolution in Microspherical Nanoscopy with Biological Objects, IEEE Proc. of National Aerospace and Electonics Conference, Dayton, Ohio, June 27-30, 4 pp., 2017.

72. V.N. Astratov, A. Brettin, F. Abolmaali, L. Poffo, and A.V. Maslov, Plasmonics and Superresolution in Microspherical Nanoscopy, IEEE Proc. of Int. Conf. on Transparent Opt. Networks – ICTON'18, Bucharest, Romania, July 1-5, 2018, 4pp.

73. A. Brettin, C.L. McGinnis, F. Abolmaali, N.I. Limberopoulos, D. Walker, A.M. Urbas, L. Poffo, A.V. Maslov, and V.N. Astratov, Superresolution Imaging of Fluorescent Nanospheres by Using High-Index Microspheres Embedded in Slabs with Illumination Provided by Plasmonic Array, IEEE Proc. of National Aerospace and Electonics Conference, Dayton, Ohio, July 23-26, 3 pp., 2018.

74. F. Abolmaali, L. Poffo, A. Brettin, D.E. Walker, N.I. Limberopoulos, I. Anisimov, A.M. Urbas, A.V. Maslov, and V.N. Astratov, Observation of the Resonantly Enhanced Resolution of Imaging of Fluorescent Nanospheres due to thir Coupling to the Metallic Nanoplasmonic Arrays, IEEE Proc. of National Aerospace and Electonics Conference, Dayton, Ohio, July 23-26, 4 pp., 2018.

75. V.N. Astratov, F. Abolmaali, A. Brettin, G.W. Bidney, B. Jin, N.I. Limberopoulos, D.E. Walker, H. Li, and A.V. Maslov, Resolution Enhancement in Microspherical Nanoscopy by Coupling of Emission to Plasmonics Metasurfaces, IEEE Proc. of Int. Conf. on Transparent Opt. Networks – ICTON'19, Angers, France, July 9-16, 4pp., 2019.

76. Mason, Daniel R., et al. "Enhanced Resolution beyond the Abbe Diffraction Limit with Wavelength-Scale Solid Immersion Lenses." Optics Letters, vol. 35, no. 12, 2010, pp. 2007–09, https://doi.org/10.1364/OL.35.002007.

77. Z. Wang, W. Guo, L. Li, B. Lukyanchuk, A. Khan, Z. Liu, Z. Chen, and M. Hong, Nat. Commun. 2,218 (2011).

78. N. Astratov and A. Darafsheh, "Methods and systems for superresolution optical imaging using high-index of refraction microspheres and microcylinders," U.S. patent application 2014/0355108 A1 published on December 4, 2014, related to U.S. provisional application 61/656,710 filed on June 7, 2012; available at http://www.freepatentsonline.com/ 20140355108.pdf.

79. A. Darafsheh, G. F. Walsh, L. D. Negro, and V. N. Astratov, Appl. Phys. Lett. 101, 141128 (2012).

80. A. Darafsheh, N. I. Limberopoulos, J. S. Derov, D. E. Walker, Jr., and V. N. Astratov, Appl. Phys. Lett. 104, 061117 (2014).

81. Y. Yan, L. Li, C. Feng, W. Guo, S. Lee, and M. Hong, ACS Nano 8, 1809 (2014).

82. L. Li, W. Guo, Y. Yan, S. Lee, and T. Wang, Light Sci. Appl. 2, e104 (2013).

83. H. Yang, N. Moullan, J. Auwerx, and M. A. M. Gijs, Proc. SPIE 9328, 932804 (2015).

84. S. Weisenburger and V. Sandoghdar, Contemp. Phys. 56, 123–143 (2015).

85. V. N. Astratov, K. W. Allen, N. Farahi, Y. Li, N. I. Limberopoulos, D. E. Walker, Jr., A. M. Urbas, V. Liberman, and M. Rothschild, “Optical nanoscopy with contact microlenses overcomes the diffraction limit,” SPIE Newsroom (to be published, 2016); K. W. Allen, N. Farahi, Y. Li, N. I. Limberopoulos, D. E. Walker, Jr., A. M. Urbas, and V. N. Astratov

86. A. Darafsheh, M. A. Fiddy, and V. N. Astratov, in IEEE Proceedings of the 14th International Conference on Transparent Optical Networks–ICTON’12, Coventry, England, 2-5 July 2012 (IEEE, 2012), Paper No. Tu.A6.5, DOI: https://ieeexplore.ieee.org/document/6254502

87. O. Svitelskiy, Y. Li, A. Darafsheh, M. Sumetsky, D. Carnegie, E. Rafailov, and V. N. Astratov, Opt. Lett. 36, 2862 (2011). https://doi.org/10.1364/OL.36.002862

88. J. Y. Lee, B. H. Hong, W. Y. Kim, S. K. Min, Y. Kim, M. V. Jouravlev, R. Bose, K. S. Kim, I.-C. Hwang, L. J. Kaufman, C. W. Wong, P. Kim, and K. S. Kim, Nature 460, 498 (2009). https://doi.org/10.1038/nature08173

89. Z. Wang, W. Guo, L. Li, B. Luk'yanchuk, A. Khan, Z. Liu, Z. Chen, and M. Hong, Nat. Commun. 2, 218 (2011). https://doi.org/10.1038/ncomms1211

90. X. Hao, C. Kuang, X. Liu, H. Zhang, and Y. Li, Appl. Phys. Lett. 99, 203102 (2011). https://doi.org/10.1063/1.3662010

91. Z. J. Smith, K. Chu, A. R. Espenson, M. Rahimzadeh, A. Gryshuk, M. Molinaro, et al., "Cell-phone-based platform for biomedical device development and education applications", PLoS ONE, vol. 6, pp. e17150, 2011.

92. N. A. Switz., M. V. D’Ambrosio and D. A. Fletcher, "Low-cost mobile phone microscopy with a reversed mobile phone camera lens", PLoS ONE, vol. 9, pp. e95330, 2014.

93. C. Vietz, M. L. Schütte, Q. Wei, L. Richter, B. Lalkens, A. Ozcan, et al., "Benchmarking smartphone fluoresence-based microscopy with DNA origami nanobeads: Reducing the gap toward single-molecule sensitivity", ACS Omega, vol. 4, pp. 637-642, 2019.

94. E. McLeod, Q. Wei and A. Ozcan, "Democratization of nanoscale imaging and sensing tools using photonics", Anal. Chem, vol. 87, pp. 6434-6445, 2015.

95. H. Zhu, O. Yaglidere, T. Su, D. Tseng and A. Ozcan, "Cost-effective and compact wide-field fluorescent imaging on a cellphone", The Royal Society of Chemistry, vol. 11, pp. 315-322, 2011.

96. Q. Wei, H. Qi, W. Luo, D. Tseng, S. J. Ki, Z. Wan, et al., "Fluorescent imaging of single nanoparticles and viruses on a smart phone", ACS Nano, vol. 7, pp. 9147-9155, 2013.

97. V. N. Astratov, K. W. Allen, N. Farahi, Y. Li, N. I. Limberopoulos, D. E. Walker, et al., "Optical nanoscopy with contact microlenses overcomes the diffraction limit", SPIE Newsroom, February 2016.
98. K. W. Allen, Y. Li and V. N. Astratov, "Comment on ‘Super-resolution microscopy by movable thin-films with embedded microspheres: Resolution analysis’ [Ann. Phys. (Berlin) 527 513 (2015)]", Ann. Phys, vol. 528, pp. 901-904, 2016.

99. Jouravlev, M. V. “Formation of Optical Fields of Stimulated Raman Scattering with a Resolution beyond the Abbe Diffraction Limit by Spherical Microlens Cavities with Whispering Gallery Modes: Near-Field Approximation.” Optics and Spectroscopy, vol. 112, no. 4, 2012, pp. 624–30, https://doi.org/10.1134/S0030400X12030253.

100. V. N. Astratov and A. Darafsheh, "Methods and systems for superresolution optical imaging using high-index of refraction microspheres and microcylinders", U.S. patent 9726874B2, [online] Available: https://www.google.com/patents/US20140355108.

101. A.V. Maslov and V.N. Astratov, "Theoretical foundations of superresolution in microspherical nanoscopy" in Label-Free Supe-Resolution Microscopy Springer Series in Biological and Medical Physics Biomedical Engineering, Switzerland:Springer, 2019.

102. Springer Series in Biological and Medical Physics Biomedical Engineering, 2019, [online] Available: https://www.springer.com/gp/book/9783030217211.

103. Z. Wang and B. Luk'yanchuk, "Super-resolution imaging and microscopy by dielectric particle-lenses" in Label-Free Supe-Resolution Microscopy Springer Series in Biological and Medical Physics Biomedical Engineering, Switzerland:Springer, 2019.

104. S. Perrin, S. Lecler and P. Montgomery, "Microsphere-assisted interference microscopy" in Label-Free Supe-Resolution Microscopy Springer Series in Biological and Medical Physics Biomedical Engineering, Switzerland:Springer, 2019.

105. A. Darafsheh, G. F. Walsh, L. Dal Negro and V. N. Astratov, "Optical super-resolution by high-index liquid-immersed microspheres", Appl. Phys. Lett, vol. 101, pp. 141128, 2012.

106. K. W. Allen, N. Farahi, Y. Li, N. I. Limberopoulos, D. E. Walker, A. M. Urbas, et al., "Super-resolution microscopy by movable thin-films with embedded microspheres: Resolution analysis", Ann. Phys. (Berlin), vol. 527, pp. 513-522, 2015.

107. K. W. Allen, N. Farahi, Y. Li, N. I. Limberopoulos, D. E. Walker, A. M. Urbas, et al., "Overcoming the diffraction limit of imaging nanoplasmonic arrays by microspheres and microfibers", Opt. Express, vol. 23, no. 19, pp. 24484-24496, 2015.

108. “Super-Resolution Microscopy Methods and Systems Enhanced by Arrays of Superlenses With Wide Field-Of-View.” Targeted News Service, Targeted News Service, 2023.

109. V. N. Astratov, A. V. Maslov, A. Brettin, K. F. Blanchette, Y. E. Nesmelov, N. I. Limberopoulos, et al., "Contact microspherical nanoscopy: From fundamentals to biomedical applications", Proc. SPIE 10077, pp. 100770S, 2017.

110. A. Bezryadina, J. Li, J. Zhao, A. Kothambawala, J. Ponsetto, E. Huang, et al., "Localized plasmonic structured illumination microscopy with an optically trapped microlens", Nanoscale, vol. 9, pp. 14907-14912, 2017.

111. Z. Wang, W. Guo, L. Li, B. Luk’yanchuk, A. Khan, Z. Liu, et al., "Optical virtual imaging at 50 nm lateral resolution with a white-light nanoscope", Nat. Commun., vol. 2, pp. 218, 2011.

112. Kim, Taekyung, et al. “Replication of High Refractive Index Glass Microlens Array by Imprinting in Conjunction with Laser Assisted Rapid Surface Heating for High Resolution Confocal Microscopy Imaging.” Optics Express, vol. 27, no. 13, 2019, pp. 18869–82, https://doi.org/10.1364/OE.27.018869.

113. Lai, Hok Sum Sam, et al. “Super-Resolution Real Imaging in Microsphere-Assisted Microscopy.” PloS One, vol. 11, no. 10, 2016, pp. e0165194–e0165194, https://doi.org/10.1371/journal.pone.0165194.

114. Wang, Zengbo, et al. “Optical Virtual Imaging at 50 Nm Lateral Resolution with a White-Light Nanoscope.” Nature Communications, vol. 2, no. 1, 2011, pp. 218–218, https://doi.org/10.1038/ncomms1211.

115. Darafsheh, Arash, et al. “Advantages of Microsphere-Assisted Super-Resolution Imaging Technique over Solid Immersion Lens and Confocal Microscopies.” Applied Physics Letters, vol. 104, no. 6, 2014, pp. 061117-, https://doi.org/10.1063/1.4864760.

116. Li, Jinxing, et al. “Swimming Microrobot Optical Nanoscopy.” Nano Letters, vol. 16, no. 10, 2016, pp. 6604–09, https://doi.org/10.1021/acs.nanolett.6b03303.

117. Bañas, Andrew, et al. Fabrication and Optical Trapping of Handling Structures for Re-Configurable Microsphere Magnifiers. SPIE, 2013, pp. 86370Y-86370Y – 5, https://doi.org/10.1117/12.2003752.

118. Lee, J. Y. et al. Near-field focusing and magnification through self-assembled nanoscale spherical lenses. Nature 460, 498–501 (2009).

119. Li, Pan, et al. “Advances in Dielectric Microspherical Lens Nanoscopy: Label-Free Superresolution Imaging.” IEEE Nanotechnology Magazine, vol. 15, no. 1, IEEE, 2021, pp. 38-C3, https://doi.org/10.1109/MNANO.2020.3037433.

120. W. V. Houston, “A compound interferometer for fine structure work,” Physical Review, 29(3), 478-484 (1927).

121. Yager, Paul, et al. “Point-of-Care Diagnostics for Global Health.” Annual Review of Biomedical Engineering, vol. 10, no. 1, 2008, pp. 107–44, https://doi.org/10.1146/annurev.bioeng.10.061807.160524.

122. Darafsheh, Arash. Optical Super-Resolution and Periodical Focusing Effects by Dielectric Microspheres. ProQuest Dissertations Publishing, 2013.